HHS Public Access

Author manuscript

Neuron. Author manuscript; available in PMC 2024 May 17.

Published in final edited form as:

Neuron. 2023 May 17; 111(10): 1591–1608.e4. doi:10.1016/j.neuron.2023.02.020.

Choroid plexus targeted NKCC1 overexpression to treat post-hemorrhagic hydrocephalus

Cameron Sadegh[1,2,*], **Huixin Xu**[1,*], **Jason Sutin**[3], **Benoit Fatou**[1], **Suhasini Gupta**[1], **Aja Pragana**[1], **Milo Taylor**[1,5], **Peter N. Kalugin**[1,6,7], **Miriam E. Zawadzki**[1,6,8], **Osama Alturkistani**[4], **Frederick B. Shipley**[1,9], **Neil Dani**[1], **Ryann M. Fame**[1], **Zainab Wurie**[1], **Pratik Talati**[2], **Riana L. Schleicher**[10], **Eric M. Klein**[11], **Yong Zhang**[12], **Michael J. Holtzman**[12], **Christopher I. Moore**[11], **Pei-Yi Lin**[3], **Aman B. Patel**[2], **Benjamin C. Warf**[13], **W. Taylor Kimberly**[10], **Hanno Steen**[1,14], **Mark L. Andermann**[7,9,15], **Maria K. Lehtinen**[1,7,8,9,16]

[1]Department of Pathology, Boston Children's Hospital, Boston, MA, 02115, USA

[2]Department of Neurosurgery, Massachusetts General Hospital and Harvard Medical School, Boston, MA, 02114, USA

[3]Fetal-Neonatal Neuroimaging and Developmental Science Center, Boston Children's Hospital, Harvard Medical School, Boston, MA, 02115, USA

[4]Cellular Imaging Core, Boston Children's Hospital, Boston, MA, 02115, USA

[5]Harvard College, Harvard University, Cambridge, MA, 02138, USA

[6]Harvard/MIT MD-PhD Program, Harvard Medical School, Boston, MA, 02115, USA

[7]Graduate Program in Neuroscience, Harvard Medical School, Boston, MA, 02115, USA

[8]Graduate Program in Biological and Biomedical Sciences, Harvard Medical School, Boston, MA, 02115, USA

[9]Graduate Program in Biophysics, Harvard University, Cambridge, MA, 02138, USA

Correspondence: maria.lehtinen@childrens.harvard.edu.

*These authors contributed equally.

AUTHOR CONTRIBUTIONS

C.S., H.X., and M.K.L. conceptualized and designed the study; C.S., H.X., J.S., B.C.W., F.B.S., N.D., E.M.K., C.I.M., M.L.A. and M.K.L. established methodology; C.S., H.X., J.S., O.A., P.N.K., S.G., A.P., B.F., Z.W., R.M.F., M.E.Z., conducted experiments; C.S., H.X., J.S., M.T., B.F., F.B.S., P.N.K., and M.L.A. analyzed data; P.T., R.L.S., Y.Z., M.J.H., A.B.P., and W.T.K., provided experimental material; P-Y.L., H.S., B.C.W., M.K.L. provided funding; M.K.L. supervised the study; C.S., H.X., and M.K.L. wrote the manuscript. All co-authors read and approved the manuscript.

DECLARATION OF INTERESTS

M.K.L., R.M.F., C.S., and H.X. are co-inventors on a provisional patent application related to this manuscript.

INCLUSION AND DIVERSITY

One or more of the authors of this paper self-identifies as an underrepresented ethnic minority in their field of research or within their geographical location. One or more of the authors of this paper self-identifies as a member of the LGBTQIA+ community. One or more of the authors of this paper received support from a program designed to increase minority representation in their field of research.

[10]Department of Neurology, Massachusetts General Hospital and Harvard Medical School, Boston, MA, 02114, USA

[11]Carney Institute for Brain Science, Brown University, Providence, RI, 02912, USA

[12]Pulmonary and Critical Care Medicine, Department of Medicine, Washington University, St. Louis, MO, 63110, USA

[13]Department of Neurosurgery, Boston Children's Hospital, Boston, MA, 02115, USA

[14]Precision Vaccines Program, Boston Children's Hospital, Boston, MA, 02115 USA

[15]Division of Endocrinology, Diabetes, and Metabolism, Department of Medicine, Beth Israel Deaconess Medical Center, Boston, MA, 02215, USA

[16]Lead contact

SUMMARY

Post-hemorrhagic hydrocephalus (PHH) refers to a life-threatening accumulation of cerebrospinal fluid (CSF) that occurs following intraventricular hemorrhage (IVH). An incomplete understanding of this variably progressive condition has hampered the development of new therapies beyond serial neurosurgical interventions. Here we show a key role for the bi-directional Na-K-Cl cotransporter, NKCC1, in the choroid plexus (ChP) to mitigate PHH. Mimicking IVH with intraventricular blood led to increased CSF [K^+] and triggered cytosolic calcium activity in ChP epithelial cells which was followed by NKCC1 activation. ChP-targeted adeno-associated viral (AAV)-NKCC1 prevented blood-induced ventriculomegaly and led to persistently increased CSF clearance capacity. These data demonstrate that intraventricular blood triggered a transchoroidal, NKCC1-dependent CSF clearance mechanism. Inactive, phosphodeficient AAV-NKCC1-NT51 failed to mitigate ventriculomegaly. Excessive CSF [K^+] fluctuations correlated with permanent shunting outcome in humans following hemorrhagic stroke, suggesting targeted gene therapy as a potential treatment to mitigate intracranial fluid accumulation following hemorrhage.

Graphical Abstract

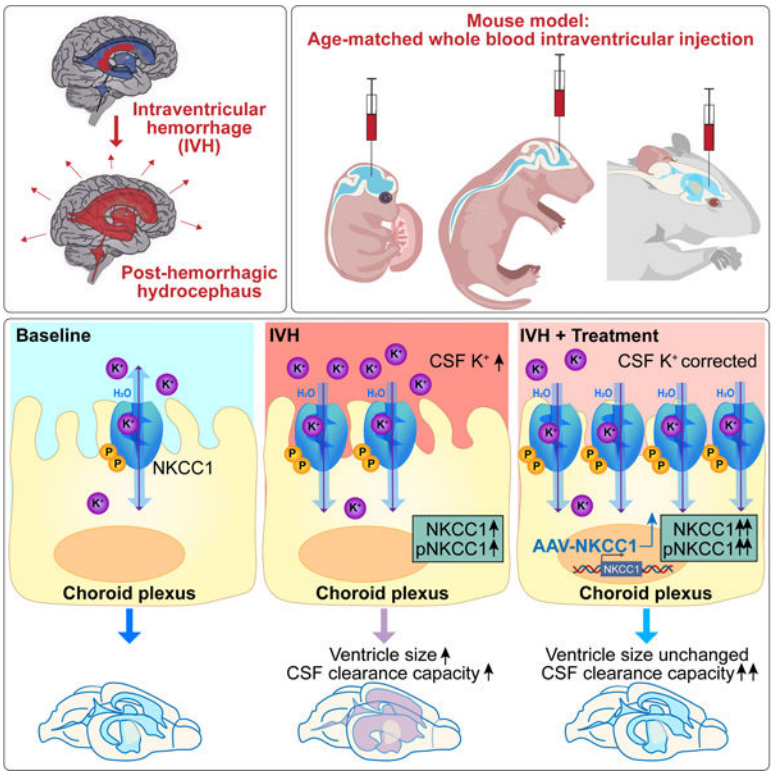

eTOC blurb

Intraventricular blood leads to increased CSF-K^+, choroid plexus (ChP) calcium activity, and increased NKCC1 expression / activation. Elevated CSF-K^+ reverses ChP-NKCC1 transport direction. In turn, ChP-NKCC1 overexpression reduces CSF-K^+, enhances CSF clearance, and prevents ventriculomegaly. Thus, ChP-targeted NKCC1 gene therapy prevents key neurological sequelae of post-hemorrhagic hydrocephalus modelled in mouse.

INTRODUCTION

Intraventricular hemorrhage (IVH) following hemorrhagic stroke is a common cause of post-hemorrhagic hydrocephalus (PHH), an excessive accumulation of cerebrospinal fluid (CSF). Accounting for nearly a quarter of PHH cases, IVH is the leading etiology of pediatric hydrocephalus in North America[1] and represents one of the most devastating complications of preterm birth.[2,3] Approximately 20% of infants with IVH develop PHH and this permanent disruption of CSF homeostasis requires neurosurgical intervention to improve CSF clearance, either by endoscopic third ventriculostomy or permanent ventricular shunting;[4,5] adults with IVH have a similar rate of surgical intervention.[6] Patients with permanent shunts require surgical procedures throughout life, which encumbers their families and strains the healthcare system.[7,8] Over 80% of severe cases develop cerebral palsy, epilepsy, or other neurologic impairments.[9,10]

As the principal brain structure that regulates CSF, the choroid plexus (ChP) represents a promising target for the treatment of PHH. Located within each brain ventricle, the

ChP forms the dominant physiologic interface between the bloodstream and CSF. The human ChP and its microvilli have a total surface area up to 50% of the blood-brain barrier.[11–13] This large ChP epithelial surface area provides unique opportunities for central nervous system (CNS) surveillance[14] and regulation of CSF volume and composition, based on mechanisms that control water and ion fluxes.[15,16] The ChP can be manipulated using adeno-associated viral (AAV)-based gene therapy.[17–19] Targeted transduction of ChP, sometimes together with other CSF-contacting cells including ependyma, provides cell type specificity, and has been shown to improve neurologic symptoms in rodent models of lysosomal storage disorders, Alzheimer's disease, Huntington's disease, and toxicity of chemotherapy, suggesting that the ChP is a viable target for sustained therapeutics for the CNS.[20–23] Therefore, genetic manipulation of the ChP represents a favorable methodology for new therapies to correct CSF properties including ionic homeostasis and total volume.

Multiple lines of evidence support ChP involvement in the pathogenesis of PHH.[24,25] However, the ChP and CSF regulation in general have been understudied due to technical challenges and lack of reliable techniques to evaluate CSF dynamics in animal models. As a result, it is still unclear whether post-hemorrhagic CSF accumulation is a consequence of inadequate clearance, excess production (from the ChP or extra-choroidal sources), or a both. A recent study demonstrated transiently increased ventricular CSF secretion ("hypersecretion") in a rat IVH model, which coincided with activation of ion transport by the Na-K-Cl cotransporter NKCC1.[25] However, the role of NKCC1 was not clear as the direction of transport depends upon the driving force of net Na^+-K^+−$2Cl^-$ gradients, which under normal physiological conditions is near zero at the ChP epithelium-CSF interface.[26] Even small changes in ion concentrations can reverse the direction of transport and bidirectional transport has been previously proposed.[28–31] Notably, ChP NKCC1 mediates either CSF clearance or secretion at distinct developmental stages in normal mice.[27] Therefore, whether NKCC1 phosphorylation and consequent activation[32] during PHH contributes to pathologic hypersecretion or facilitates clearance of CSF as a compensatory homeostatic mechanism remains unknown.

Here, we studied the role of NKCC1 in improved mouse models of pediatric and adult IVH with acquired ventriculomegaly. We found that AAV-mediated NKCC1 overexpression in the ChP following intracerebroventricular (ICV) blood injections restored CSF ionic homeostasis, accelerated CSF clearance, and mitigated ventriculomegaly. In contrast, expression of a phosphodeficient form of NKCC1 failed to mitigate ventriculomegaly. These data suggest that inadequate CSF clearance is the primary driver of post-hemorrhagic CSF accumulation and PHH. Our findings also support the concept of the ChP as a first line of defense to restore CSF homeostasis and a favorable gene therapy target for the treatment of acute conditions such as PHH following pediatric and adult hemorrhagic stroke.

RESULTS

Improved models of IVH using age-matched blood in mice

We modified current rodent models of embryonic and neonatal IVH to better reflect the physiologic mechanisms following the human condition. In most adult rodent models of IVH and PHH,[33] autologous, fresh, and unmodified blood is used to model intraventricular

bleeding and subsequent ventriculomegaly. However, in embryonic and neonatal IVH models, the lysed red blood cells[34] or maternal blood have been more frequently used, despite the potential mismatch in donor and recipient blood composition.[35] Our proteomic analysis of mouse plasma obtained at different developmental stages revealed striking changes in the blood proteome including key coagulation factors (e.g., Kininogen-1 and Plasminogen) and inflammatory molecules (Figure S1A–G and Dataset S1). Further, in embryonic day (E) 14.5 mice, ICV injection of age-matched blood yielded more robust ventriculomegaly compared to blood from older mice (Figure S1H). Therefore, to model human pediatric IVH, we used ICV injections of age-matched blood. In addition, we employed a parallel donor/recipient surgical model to rapidly acquire unmodified allogeneic fetal blood from the same mouse strain (CD1), obviating the need for separating blood components with additives such as anti-coagulants which could, for example, interfere with calcium-dependent cell signaling and potentially trigger additional inflammation.

We studied mice at two ages, embryonic day (E)14.5 and postnatal day (P)4, which generally correspond to human CNS development at early (second trimester) and late (early third trimester) gestation, respectively[36] (Figure 1A). The E14.5 model represents hemorrhage that occurs early in development (as early as 12GW in human fetus), which accounts for about 10–20% of idiopathic hydrocephalus cases.[37,38] The P4 model corresponds to the time when preterm infants are most vulnerable to hemorrhagic strokes in the germinal matrix (early third trimester), and also coincides with the typical timing of IVH. To model moderate to severe IVH (Papile grade 3 IVH[39]), we injected volumes of blood corresponding to approximately 50% of total ventricle volume at each age (2 μL blood at E14.5; 3–5 μL blood at P4). Ventricular blood formed solid clots inside P4 brains but remained in liquid form inside E14.5 brains (Figure S1I, S1J). Red blood cells ultimately lysed in CSF, as expected (Figure S1K). In both models, the mice matured without gross anatomical changes in skull dimension (Figure 1A, Figure S1L), consistent with the majority of clinical cases. In the absence of a major externally identifiable PHH phenotype, we developed additional tools for detailed anatomic characterization and measurements of CSF dynamics.

MRI and ICP/infusion testing in models of IVH

We used fast-acquisition, T2-weighted magnetic resonance imaging (MRI) to assess ventricle volume in isoflurane-anesthetized mice approximately 3 weeks following injection of intraventricular blood at either E14.5 or P4 (Figure 1B). In both age groups intraventricular blood injection generated a nearly two-fold increase in the volume of the lateral and third ventricles as compared to control mice, which received phosphate-buffered saline (PBS) 3 weeks following blood injection (Figure 1C, D). Ventricle volumes of control (PBS-injected) mice were not different from reported healthy un-injected mice of the same age.[27] Notably, the doubling of ventricle volume was not apparent by less sensitive methods, including skull size measurements (Figure S1L), classic histology (e.g., due to variability in tissue preparation), or post-perfusion brain MRI (e.g., due to loss of intracranial pressure that sustains ventricle size in smaller, more compliant brains), emphasizing the utility of live animal MRI for quantification of ventricular volume.

We used a miniaturized clinical CSF infusion test[27,40–43] to study CSF dynamics in mice (Figure 1B, 1E). Values of intracranial compliance (C_i) and CSF resistance (R_{CSF}) during infusion reflect the ability of the entire intracranial space (including brain, meninges, and CSF outflow routes) to adjust to increases in CSF volume. In our approach, a pressure sensor coupled with infusion tubing is implanted inside a mouse lateral ventricle to measure intracranial pressure (ICP), and in turn calculate, C_i, and R_{CSF}. CSF volume is increased by ICV infusion of artificial CSF (aCSF), causing ICP to rise and then plateau at a new level. The ICP trajectory provides a quantitative analysis of Ci, an indicator of the stiffness of intracranial constituents, which determines the rate at which ICP rises before it reaches a plateau at a new equilibrium under constant infusion. The total increase of ICP from baseline to plateau reflects CSF clearance capacity (termed “conductance,” related to the resistance of CSF exiting the ventricular system). When evaluated at 6–9 weeks, the baseline ICP values in control and IVH mice remained indistinguishable (Figure 1F), consistent with the lack of symptoms caused by elevated ICP, such as weight loss and impaired gait and posture.[44] Nonetheless, mice that had received intraventricular blood had approximately half the intracranial compliance of control mice (Figure 1G, S1M), indicating their brains were stiffer and did not permit an increase in CSF volume as well as healthy mice, thus reaching peak ICP much faster. The stiffening of the brain is in agreement with clinical observations of scarring of ependyma and leptomeninges, causing reduced ventricular compliance in hydrocephalus.[33] Strikingly, CSF clearance, as evaluated by conductance, was *increased* by two-fold in our IVH model (Figure 1H). We can infer that for the ventriculomegaly to occur, the observed increase in CSF clearance must have been offset by excessive CSF production (“hypersecretion”) by likely extra-choroidal sources of CSF.[45] Hypersecretion associated with increased ventricular volume is consistent with previous descriptions in humans with ChP hyperplasia[46] and in a rat model of PHH,[25] but the exact mechanisms leading to CSF hypersecretion remain to be elucidated.

Inflammation resulting from experimental procedures was unlikely to contribute to these findings. Microglial activation was restricted to the immediate proximity of the ICV injection site in brain parenchyma at P7 (Figure 1I). In addition, no substantial microglial changes were observed at the catheter insertion site during the approximately 30-minute infusion period for the constant rate infusion test (Figure 1I). Overall, these data match prior histological analyses performed in conjunction with cannula insertion into the lateral ventricles demonstrating that the brain recovers from surgery without evidence of persistent inflammation.[14] Taken together, our data from pediatric IVH mouse models suggest that intraventricular blood leads to mild ventriculomegaly compensated by increased CSF clearance, which mimics the expected clinical sequelae for a majority of post-IVH patients who do not develop severe symptoms of hydrocephalus.

Lateral ventricle ChP responds rapidly to intraventricular blood

Further experiments revealed that the ChP responds to intraventricular blood with cytosolic calcium spikes within seconds, to changes in protein phosphorylation within days, consistent with a role in surveilling CSF composition. As is the case for many cell types, cytosolic calcium spikes are an early sign of activation of ChP epithelial cells.[14] Increases in calcium activity are readily seen in response to neurotransmitters in the CSF.[14,47] Therefore, we

evaluated *ex vivo* ChP calcium responses following epithelial contact with blood plasma. E14.5 ChP explants derived from *FoxJ1-Cre::GCaMP6f* transgenic mice were affixed to glass coverslips and incubated in aCSF to allow live cytosolic calcium imaging of *FoxJ1*-expressing ChP epithelial cells[14] during focal blood application (Figure 2A). Cytosolic calcium levels in ChP epithelial cells rapidly increased in response to application of cell-free blood plasma (Figure 2B, Video S1–2; similar data were obtained with cell-free blood serum, not shown). Cell segmentation (using morphological filters) and extraction of calcium activity time courses confirmed that > 90% of epithelial cells were activated in response to plasma (Figure 2B–C). This finding of simultaneous activation of nearly all epithelial cells allowed us to analyze bulk signals as a surrogate for individual cellular activities, thereby facilitating evaluation of overall ChP tissue responses to blood (Figure 2D–E).

IVH induces NKCC1 expression/phosphorylation and leads to transiently elevated CSF [K^+]

Rapid calcium responses of ChP epithelial cells were followed by increased expression of NKCC1 and robust phosphorylation and consequent activation of NKCC1 in E14.5 and P4 ChP 48 hours following IVH. The pNKCC1 to total NKCC1 ratio was not significantly changed (PBS vs. IVH = 1.000 ± 0.107 vs. 1.006 ± 0.286, all values normalized to corresponding PBS controls) (Figure 2F–H). Elevated NKCC1 activity at the ChP could increase or decrease ventricular CSF volume depending upon the direction of transport, which is determined by the combined gradients of Na^+, K^+, and Cl^-, with changes in extracellular K^+ having a strong influence due to the very low levels at baseline. We measured these ions in the CSF 48 hours following IVH using the P4 age group, and observed a significant, transient elevation in CSF [K^+] (Figure 2I), while the total osmolarity at each time point remained unchanged between IVH mice and controls (Figure 2J). The timing of post-hemorrhagic increases in CSF [K^+] coincided with a transient increase in ChP NKCC1 expression and phosphorylation. This finding supports the hypothesis that NKCC1 normalizes CSF K^+ by increasing active transport of K^+ (and its other substrate ions), paralleled by net diffusion of water[48] across multiple pathways (likely including AQP1) from ventricular CSF into ChP epithelial cells.[15,49]

Disruption of ChP epithelial calcium signaling worsens post-hemorrhagic hydrocephalus

The instantaneous intracellular calcium responses, subsequent upregulation of phosphorylated and total NKCC1, and concurrent increase in CSF [K^+] (Figure 2) are all consistent with roles for the ChP as an immediate responder to ventricular blood and suggest that NKCC1 could mediate the observed increase in CSF clearance (Figure 1). As such, disruption of this compensatory response by the ChP would be expected to worsen IVH outcomes. We used several methods to block calcium responses[50–52] in ChP explants following focal application of age-matched plasma (Figure S2A, B). These methods included (1) blocking release of intracellular calcium stores by disrupting 1,4,5-trisphosphate (IP3) signaling with lithium chloride (LiCl) or by directly inhibiting the IP3 receptor with 2-aminoethoxydiphenyl borate (2-APB), and (2) abolishing extracellular calcium influx by chelation with ethylenediaminetetraacetic acid (EDTA) or ethylene glycol-bis (β-aminoethyl ether)-N,N,N’,N’-tetraacetic acid (EGTA). After confirming the effectiveness of these methods (Figure S2A, B), we tested the effect of disrupting ChP

calcium activity *in vivo* on NKCC1 phosphorylation following IVH. We pre-treated adult mice with ICV LiCl (50 mM, 5 μL) 30 minutes prior to intraventricular blood exposure followed by measurement of pNKCC1 48 hrs later. LiCl pre-treatment decreased NKCC1 phosphorylation under these conditions, possibly due to a decrease in the phosphorylation of SPAK (Figure S2C, S2D), an upstream kinase known to phosphorylate NKCC1.[25]

We next asked whether disruption of ChP epithelial cell calcium responses would impair compensatory CSF clearance in our IVH model. We pretreated E14.5 embryos with ICV LiCl 30 minutes prior to intraventricular blood or PBS injection and evaluated postnatal mice for hydrocephalic phenotypes by MRI and by a CSF infusion test, as described above (Figure S2E). Mice receiving intraventricular blood that were pre-treated with LiCl had more pronounced ventriculomegaly as compared to controls, including two extreme cases with over 200-fold ventricular enlargement (Figure S2F). CSF infusion testing revealed a decreased, rather than increased, CSF clearance capacity in ICV LiCl+blood mice compared to ICV LiCl+PBS mice (Figure S2G). Baseline ICP was unaltered (LiCl+PBS 6.394 ± 1.559 mm Hg, N = 5, LiCl+IVH 6.407 ± 2.105 mm Hg, N = 8, $p = 0.9900$; Welch's two-tailed unpaired t-test). In cases of severe ventriculomegaly, ICP is technically difficult to ascertain (despite acquisition of long baseline recordings to identify the true baseline ICP) because of the potential for significant loss of CSF while placing the catheter. LiCl treatment alone did not affect ventricle size (LiCl + PBS: 0.91 ± 0.22 mm^3, N=7 vs. PBS alone: 1.01 ± 0.34 mm^3, N=9) or other CSF dynamics. While the exact molecular mechanisms remain to be elucidated, these findings are consistent with a severe reduction in CSF clearance due to mitigated NKCC1 phosphorylation and suggest that ChP responses to IVH may be necessary for the subsequent activation of NKCC1. These data support the importance of ChP epithelial calcium signaling for the maintenance of reduced ventricle size in the setting of IVH.

AAV-NKCC1 tissue specificity and duration of expression

We hypothesized that ChP NKCC1 augmentation may improve the ChP response to IVH. When delivered ICV at P5, AAV-NKCC1 expression, identified by its HA-tag to distinguish from endogenous NKCC1, was detected predominantly on the apical, CSF-facing surface of ChP epithelial cells 48 hours later at P7 (Figure 3A, Figure S3). We used the AAV2/5 serotype, which when delivered ICV, has tropism for ChP epithelial cells with minimal expression elsewhere in the CNS (Figures 3A, B and S3A–H).[19,27] ChP Immunoblotting confirmed increases of both total NKCC1 and pNKCC1 (Figure 3C–E). While expression of the HA-tag associated with AAV-NKCC1 remained detectable at 3 weeks, we did not observe persistently increased pNKCC1 or total NKCC1 expression compared to controls at 3 weeks and 9 weeks following IVH (Figure 3C–E and S3D–H). These data suggest that the increase in NKCC1 expression by AAV is transient during the neonatal developmental period when endogenous NKCC1 expression levels are naturally lower. Transient NKCC1 overexpression was likely due to the large size of NKCC1.[53] As development progresses, endogenous NKCC1 expression also steadily increases to eventually reach adult levels.[27]

ChP targeted NKCC1 overexpression reduces ventriculomegaly in pediatric IVH models

We hypothesized that AAV-NKCC1 would provide targeted augmentation of ChP activity in response to IVH in our models of pediatric PHH. We first introduced intraventricular blood in pups at P4, and then delivered AAV-NKCC1 or control AAV-GFP (Green fluorescent protein) into the same lateral ventricle 24 hours later at P5 (Figure 3F). We evaluated IVH mice receiving AAV-NKCC1 vs. AAV-GFP control by MRI (2–3 weeks later) and fluid dynamics testing (6–9 weeks later) (Figure 3F). ChP NKCC1-overexpressing mice had smaller ventricles compared to their AAV-GFP injected littermates following intraventricular blood exposure (Figure 3G–I). Ventricle volumes of ChP NKCC1-overexpressing IVH mice were similar to those of healthy naive mice or sham controls receiving only PBS (Figure 1D), indicating that overexpression of NKCC1 fully rescued the blood-induced ventriculomegaly normally seen in IVH animals. NKCC1 overexpressing mice did not show any change in ICP. Notably, NKCC1 augmentation was accompanied by even higher CSF clearance capacity compared to GFP control mice at two months following IVH (Figure 3J–K). NKCC1 overexpression retained CSF [K^+] at baseline levels compared to controls (Figure 3L; raw values provided in Figure S3S; age-matched, naive P7 animals: 4.36 ± 0.92 mM,[27] P25 animals measured in the same ICP-OES assay: 3.056 ± 0.625 mM (Figure 2I)), consistent with NKCC1 mediating CSF clearance by ion transport and an associated net movement of water. These data demonstrate that NKCC1 overexpression acutely mitigates ventriculomegaly and CSF [K^+] and leads to persistently increased CSF clearance.

Supporting the concept that ChP-NKCC1 is protective in PHH, we found that an increase in baseline ChP NKCC1 availability by *in utero* overexpression (Figure S3I–J) also enabled a more favorable ventricular response to IVH at P4. We evaluated ventricle sizes (2–3 weeks later) and capacity for CSF clearance (6–9 weeks later). ChP NKCC1 overexpressing mice showed improved ventricle phenotypes in response to IVH compared to mice receiving PBS (Figure S3K–O). Importantly, NKCC1 overexpressing mice with IVH had ventricle volumes similar to wild-type mice receiving PBS (Figure 1D). They were also protected from blood-induced decreases in intracranial compliance (Figure S3P) in comparison to wild-type mice (Figure 1F) and had a consistently increased capacity for CSF clearance without changes in ICP following intraventricular blood exposure (Figure S3Q–R). These results suggest that following IVH, the therapeutic overexpression of NKCC1 initially facilitates ChP ion and fluid transport and is accompanied by longer term benefits that perhaps involve non-choroidal aspects of fluid handling in the brain.

We next tested the overexpression of a phosphodeficient form of NKCC1 (NT51[54]) to determine whether NKCC1 overexpression required physiologic activation via phosphorylation. In NKCC1-NT51, serine and threonine residues located in the N-terminal phosphoregulatory domain typically required to be phosphorylated for NKCC1 activation are mutated to silent, charge-equivalent amino acids, rendering NKCC1 inactive[54] (Figure 4A). We validated AAV-NKCC1-NT51 expression on the apical surface of ChP epithelial cells by its FLAG tag in neonatal mice (Figure 4B). We confirmed that AAV-NKCC1-NT51 augmentation did not increase pNKCC1 compared to wild-type AAV-NKCC1 (Figure 4C–E). Importantly, when AAV-NKCC1-NT51 was delivered to neonates at P5, 24 hours following IVH at P4, AAV-NKCC1-NT51 failed to mitigate ventriculomegaly

when evaluated 3 weeks later by MRI (Figure 4F, G). AAV-NKCC1-NT51 also failed to facilitate CSF-K^+ clearance when compared to wild-type AAV-NKCC1 (Figure 4H). These data demonstrate that together with increased CSF [K^+], NKCC1 expression and activation by upstream protein kinases is required to mitigate ventriculomegaly.

ChP responds rapidly to IVH in vivo

Developmental age at the time of IVH may factor into whether NKCC1 augmentation confers a beneficial response to IVH, as NKCC1 expression and phosphorylation is tightly regulated during late embryonic and early postnatal development.[27] Therefore, we tested our model also in adult mice (8–10 weeks). We used a recently developed *in vivo* ChP imaging approach[14] to record ChP calcium activity through a transcortical cranial window in awake, head-fixed adult mice. We adapted this surgical protocol to include the placement of an injection cannula into the contralateral ventricle for direct ICV delivery of reagents during live imaging of the ipsilateral ChP (Figure 5A, Figure S4A–B). We observed robust and rapid increases in ChP cytosolic calcium activity following intraventricular infusion of serum (Figures 5B–E, S4C, Video S3; similar observations followed plasma infusion, not shown), consistent with findings in E14.5 ChP explants (Figure 2). In control experiments in which we infused aCSF *in vivo* and *in vitro*, we further confirmed that the changes in calcium were not due to mechanical fluid movement or potential osmolarity changes introduced by serum or plasma (Figure S4D–I).

Using a cannula that allowed us to perform repeated CSF constant rate infusion tests following IVH (Figure 5F) we were able to investigate changes in CSF dynamics longitudinally after intraventricular blood exposure This approach provided a level of temporal resolution that was not possible with our pediatric models (Figure 1).We first observed a decrease in CSF clearance capacity 3 days after intraventricular blood exposure (as expected based on clinical observations), followed by a steady increase in CSF clearance capacity over six weeks (Figure 5G),

ChP targeted NKCC1 overexpression prevents ventriculomegaly in a model of adult IVH

We conducted serial live MRI scans to track ventricle size1, 2, 3, 6, and 13 days following delivery of age-matched intraventricular blood. AAV-NKCC1 or control AAV-GFP was introduced 2 days after intraventricular blood (Figure 5H; immediately following the MRI session on Day 2) so that the severity of ventriculomegaly between the two groups was similar. We observed continuous enlargement of the lateral ventricles from Day 1 to Day 2 in both groups, consistent with previous studies in adult rodent models.[24,25] By Day 3, only 24 hrs following AAV injection, the mice that received AAV-NKCC1 demonstrated a reduction in lateral ventricle volumes (Figure 5I–J). Importantly, these AAV-NKCC1 mice maintained the reduction in ventricle volumes over two-weeks following intraventricular blood exposure, as compared to control animals (Figure 5J), suggesting sustained prevention of ventriculomegaly attributable to NKCC1 overexpression. Collectively, the results of experiments using this adult model of IVH validate the utility of AAV-NKCC1 to target ChP epithelial cells as a possible gene therapy for PHH and broaden its potential applicability across pediatric and adult ages.

Identification of CSF ionic disequilibrium following PHH in humans

Some of the observations in our animal models lead to specific predictions on how CSF composition might be altered in the human condition. CSF samples from adult patients with aneurysmal subarachnoid hemorrhage (aSAH) were acquired from a published prospective single-center cohort study.[55,56] These patients were afflicted by hemorrhagic stroke due to the acute rupture of an intracranial aneurysm, with subsequent IVH and acute PHH that was treated by placement of an ICV catheter (clinically referred to as an external ventricular drain). CSF was collected at 3 – 6 day intervals between serial samplings for up to 16 days, totaling 54 unique CSF samples from 20 patients. The outcomes were recorded as either resolution of hydrocephalus (ICV catheter removal) or persistence of hydrocephalus (permanent shunt placement) (Figure 6A–B). Patient demographics, illness severity, and time of collection were similar between the two groups (Figure S5A–D).

We observed CSF hypo-osmolarity in 60% of patients (mean ± SEM.; 201 ± 16 mEq / L) despite the presence of normal serum osmolarity measurements (acquired in the same patients) (Figure 6C–D), a phenomenon not reported previously and possibly reflecting failure of CSF ionic homeostasis following IVH. To take total osmolarity into account, we defined relative CSF $[K^+]$ (mEq / L) as a percentage of total osmolarity (mEq / L). We found that, although absolute CSF $[K^+]$ remained within normal limits for all patients (Figure 6E) and showed no correlation to initial IVH volume (Figure S5E), the relative CSF $[K^+]$ was significantly higher in patients requiring shunt surgery vs. those whose hydrocephalus had resolved (1.20 vs. 1.06%, $p < 0.05$) (Figure 6F). This finding is consistent with the presence of elevated CSF $[K^+]$ observed in our mouse IVH models (Figure 2I–J). Patients requiring shunting also displayed a wider range relative CSF $[K^+]$, possibly reflecting a reduced capacity for potassium homeostasis (Figure S5F–I). Therefore, CSF $[K^+]$ and osmolarity changes may be informative metrics for CSF ionic disturbances and an indirect assessment of the ChP capacity for maintaining CSF homeostasis. Several anatomic, clinical, and radiographic factors are also associated with the need for permanent shunt surgery following aSAH,[57] but none of these factors correlated with outcomes in our cohort of patients (Figure S5J–O). Collectively, our data indicate that the CSF $[K^+]$ ionic disturbance observed in mouse models has direct translational implications and suggest that ChP management of CSF $[K^+]$ levels might correlate with surgical need in the management of PHH.

DISCUSSION

There is a dire need for new and durable treatments for the various etiologies of pediatric and adult PHH. We hypothesized that the ChP is an amenable treatment target that has a central role in rapidly restoring CSF dynamics following IVH. Here, we demonstrate a candidate ChP therapy based on overexpression of NKCC1 that decreased brain ventricular volume following IVH and prevented some of the most salient clinical features of PHH observable in mice (Figure 7). This therapeutic approach emerged from experiments using new modified mouse models of PHH and newly adapted methods to image ChP epithelial responses following blood exposure, quantify the changing intracranial capacity for CSF clearance, and specifically target the ChP using AAV to distinguish its contributions to CSF homeostasis from extra-choroidal sources.

While the ChP is commonly simply described as the major source of CSF, our work (see also[27]) reveals a more versatile role for the ChP with the notable ability to bidirectionally transport solutes and thereby control net movement of water in either direction across the epithelia. Our therapeutic target, NKCC1, is a well-studied ion cotransporter with a stoichiometry of $Na^+ : K^+ : 2\ Cl^-$ [58] which is highly expressed at the apical membrane of ChP epithelial cells. Among the transported ions, CSF K^+ likely plays a critical role in determining NKCC1 transport directionality, as the K^+ concentration in the CSF is typically very low and predicted to rise as a consequence of red blood cell lysis following a bleed. Indeed, acute increases in spinal CSF [K^+] were previously found in samples from human neonates with IVH.[59]

Time and tissue specific NKCC1 phosphorylation is required for ChP-mediated CSF volume homeostasis following IVH. ChP NKCC1 is phosphorylated at early timepoints coincident with increased CSF [K+] during the acute phase of IVH, when CSF clearance is at a minimum and likely insufficient. To specifically assess choroidal NKCC1 contributions to ventricular CSF volume and ionic composition, we targeted overexpression of NKCC1 to ChP epithelia with AAVs and measured an increased post-IVH CSF clearance capacity and normalization of ventricle volume and CSF [K^+]. AAVs provide more specificity compared to pharmacologic targeting of NKCC1, which would also affect neurons, glia, and leptomeningeal vasculature in addition to ChP epithelia.[25,45,60] To control for off-target or dominant negative effects following AAV transduction,[61] we tested an inactivated form of NKCC1 (AAV-NKCC1-NT51), which harbors silent mutations in the N-terminal phosphoregulatory domain[54] and showed that this NKCC1-NT51 failed to mitigate ventriculomegaly. These findings indicate that choroidal NKCC1-mediated homeostasis is beneficial following IVH and can be augmented with targeted gene therapy. A striking corollary to these findings is that they point to extra-choroidal site(s) as likely dominant source(s) of CSF in the acute setting of hemorrhage.

We adapted the best available clinical diagnostic tools such as *in vivo* brain MRI, ICP measurements, and the constant rate infusion test to mice to investigate changes in CSF dynamics following IVH. Accordingly, these data offered insights that could have gone unnoticed using histologic methods or isolated measurements of intracranial pressure. With repeated CSF infusion tests on the same group of post-IVH mice over a time course of several days to weeks, we confirmed that ICP was normal despite reductions in intracranial compliance, which is consistent with a model of “compensated” and asymptomatic PHH. We also identified a temporarily reduced capacity for CSF clearance within days after IVH, consistent with either acute obstructive hydrocephalus or extra-choroidal CSF hypersecretion lasting one or more weeks as previously reported in rats.[25] This implies that there might be a critical and short window of opportunity to improve and hasten this compensatory response in rodent models, and perhaps a slightly different window for clinical care.

Comparing the clinical burden of IVH and mouse models may provide some insights. Humans take 1–2 weeks to clear IVH, whereas mice were able to accomplish this in 2–4 days with variable degrees of clot formation (see Figure S1) despite having a higher blood/ventricle volume ratio than in most human cases. The extent of IVH is a known

negative prognostic indicator;[62] in some settings, surgical hematoma clearance might be considered beneficial.[63–66] Therefore, the persistence of ventricular blood in humans might explain subsequent clinical "decompensation" in contrast to the mouse model. The resultant CSF ionic disequilibrium might benefit from prolonged ChP-mediated CSF clearance. To begin to examine the extent and duration of CSF ionic disequilibrium, we acquired human ventricular CSF samples from a previously studied cohort with acute PHH. We found (1) prolonged CSF ionic disturbance in humans, suggesting a potentially wider therapeutic window of up to 2 weeks; (2) perturbations in CSF osmolarity and relative $[K^+]$ that are consistent with our model of K^+-driven ionic homeostasis; and (3) possible prognostic features of CSF composition. Using serial sampling of ventricular CSF in patients, we confirmed a prolonged duration of CSF hypo-osmolarity and relatively elevated $[K^+]$ up to 2 weeks after the onset of hemorrhage. We also observed relatively higher and more fluctuating CSF $[K^+]$ in those patients that eventually required permanent ventricular shunt placement compared to those who recovered. These data may reflect either an excessive IVH burden or the insufficiency of ChP-driven counter-regulatory mechanisms over time.

Our study supports the concept that the ChP acts as an immediate responder to intraventricular blood by boosting CSF clearance capacity in the acute phase of IVH when CSF clearance is at its nadir and that this NKCC1-dependent mechanism can be targeted by AAV therapy to achieve benefits in pediatric and adult models. AAV-NKCC1 expression was transient in our study, due likely to the large size of the transgene. This feature may help focus the benefits of NKCC1 overexpression to the critical time immediately following IVH while also helping to limit any potentially undesirable long-term consequences of the approach. The ChP might not meaningfully contribute to CSF clearance at late stages of PHH and in fact may worsen symptoms when CSF [K] normalizes. Accordingly, subtotal ablation of the ChP in this chronic setting (endoscopic third ventriculostomy combined with choroid plexus cauterization; ETV/CPC), helps avoid permanent ventricular shunt surgery in certain patients.[4] However, the youngest patients with PHH (<6 months) appear to have a low rate of success with combined ETV/CPC,[71] underscoring a clinical need for alternative and individualized treatment options. Gene therapy applied alone or paired with existing short-duration treatment options (e.g., CSF removal by lumbar or trans fontanelle aspiration), may ultimately reduce the need for permanent shunting, improve clinical outcomes and quality of life, and thus reduce the burden of PHH on patients and the medical system. AAV therapy is particularly appealing for PHH due to the clinical feasibility for direct surgical access for local AAV administration to the ventricular system and to the ChP.

In addition to the ChP, tissues contributing to CSF clearance include various lymphatic pathways (dural/meningeal), cranial nerves, spinal nerve roots, major blood vessels traversing the skull base, and trans-venous pathways (arachnoid granulations).[67] Recent findings specifically implicate lymphatic drainage in clearing erythrocytes and iron in the context of IVH,[68] suggesting that this pathway might complement the role of the ChP in homeostasis following IVH. Our constant rate infusion test incorporates all CSF clearance routes and therefore leaves open the possibility that longer-term changes in CSF clearance might also be mediated by lymphatic pathways. While ChP-targeted NKCC1 gene therapy successfully rescued elevations in $[K^+]$ and ventriculomegaly in mice exposed to

intraventricular blood, future therapies may benefit from targeting both ChP (acute) and lymphatic (chronic) pathways of CSF clearance. In pediatric cases, however, the ChP may be a more important target, as studies in animal models have shown a lack of mature meningeal lymphatics until later stages in development (e.g., P12 in mice and P7 in rats).[69,70]

STAR METHODS

RESOURCE AVAILABILITY

Lead contact—Further information and requests for resources and reagents should be directed to and will be fulfilled by the Lead Contact, Maria K. Lehtinen, maria.lehtinen@childrens.harvard.edu.

Materials Availability—The AAV-NKCC1-NT51 plasmid was generated from Addgene product #49061. The YFP sequence was removed to reduce the total size of insert, and the coding sequence was cloned onto an AAV backbone supplied by Vector core at University of Pennsylvania (pENN.AAV.CMVs.RBG (no intron)). All reagents are available from the Lead Contact.

Data and Code Availability

1. Data availability: Blood proteomics data is summarized in Supplemental Data and the mass spectrometry data have been deposited to the ProteomeXchange Consortium via the PRIDE partner repository[75] with the dataset identifier PXD039738. Original western blots reported in this paper will be shared by the lead contact upon request.
2. Code availability: All code used in this study is available on GitHub. https://github.com/LehtinenLab/Xu-Sadegh-2023
3. Availability of other source data and any additional information required to reanalyze the data reported in this paper is available from the lead contact upon request.

EXPERIMENTAL MODEL AND SUBJECT DETAILS

Animal studies—All animal care and experimental procedures were approved by the Institutional Animal Care and Use Committees of Boston Children's Hospital. Animals were housed in a temperature-controlled room on a 12-hr light / 12-hr dark cycle and had free access to food and water. Mouse lines used include *FoxJ1-Cre*[76], *Ai95D* (Jax# 024105[77]), and CD-1 (Charles River Laboratories).

Mouse CSF samples—CSF was collected by inserting a glass capillary into cisterna magna and processed as described.[78] It was visually examined for purity, and samples were centrifuged at 10,000 g for 10 minutes at 4°C prior to immediate analysis or storage at −80°C.

Human CSF samples—Human CSF samples were collected from external ventricular drains at Massachusetts General Hospital, centrifuged at 2000 x *g* for 15 minutes at 4°C and frozen at −80°C until analysis. Demographic, imaging, and clinical outcomes were collected from the medical record and de-identified for research purposes.

Plasma collection for proteomics using Data-Dependent Acquisition (DDA)—Fresh blood was obtained from the jugular vein of E14.5 embryos. Adults (8 weeks) and P4 pups were anesthetized with ketamine / xylazine (dose, route), or ice, respectively, thoracotomized, and atrial blood was gently collected in EDTA coated glass microcapillary tubes (Drummond 0.4mm). Centrifugation was performed twice for 10 minutes at 5,000 g / rcf at 4°C and plasma was extracted from the supernatant. Only samples with yellow to salmon color were included; pink/red colored samples indicative of red blood cell lysis were discarded. Plasma samples were stored at −80°C until processing in LC/MS.

METHOD DETAILS

Mass spectrometry—Plasma samples were processed with an MStern blotting protocol developed as described.[80,81] In brief, 1 µl of plasma (approximately 50 µg of protein) was mixed in 100 µl of 8 M urea buffer. Cysteine residues were reduced using a final concentration of 10 mM of dithiothreitol and then alkylated with a final concentration of 50 mM of iodoacetamide. 15 µg of proteins were loaded on to a 96-well plate with a polyvinylidene fluoride membrane at the bottom (Millipore-Sigma), previously activated with 70% ethanol and primed with 8M urea buffer. Trypsin digestion was performed onto the membrane by incubation with the protease for 2 hours at 37°C. Resulting tryptic peptides were eluted with 40% acetonitrile/0.1% formic acid. A C18 clean-up of the samples was realized using a 96-well MACROSPIN C18 plate (TARGA, NestGroup) and stored at −20°C before LC/MS analysis. Samples were analyzed using a nanoLC system (Eksigent) coupled online to a Q Exactive mass spectrometer (Thermo Scientific). From each sample, 1 µg peptide material was separated using a linear gradient from 98% solvent A (0.1% formic acid in water), 2% solvent B (0.1% formic acid in acetonitrile) to 40% solvent B over 45 minutes. The mass spectrometer was operated in DDA mode, selecting up to 12 of the most intense precursor ions for further MS/MS fragmentation. Label-free protein quantitation analysis employed MaxQuant 1.5.3.30.[79,82] Raw data were downloaded and used to build a matching library and searched against the UniProt Mouse reviewed protein database. Standard search settings were employed with the following modifications: Max missed cleavage 3; fixed modification Carbamidomethylation (C); variable modification Oxidation (M)44. A revert decoy search strategy was employed to filter all proteins and peptides to <1% FDR.

Headpost, cranial window, and ICV canula placement—Mice used for *in vivo* two-photon imaging (8–20 weeks) were outfitted with a headpost and a 3 mm cranial window, as previously described.[14] In addition to the trans-frontal bone cranial window, a contralateral trans-occipital approach to cannula insertion was developed to enable simultaneous ICV injections and two-photon imaging. The trans-occipital injection cannula was inserted through a drill hole placed in the superior- and lateral-most border of the suboccipital bone and advanced to a lateral ventricle target (stereotaxic coordinates: 0.4 mm posterior

to bregma, 1.0 mm lateral to the midline, and 2.0 mm in depth from the brain surface). A dummy cannula (stylet that has the same diameter as the inside of the cannula and helps prevent CSF leakage or infection) was inserted and held in place with a screwcap to prevent infection and tissue growth into the cannula. This dummy cannula was removed prior to ICV injections. The steel cannula was then fixed to the titanium headpost and cranial window using dental cement.

Calcium imaging and analysis—Two-photon microscopy (Olympus FVMPE-RS two-photon microscope; 30.0 frames / s; 512 × 512 pixels / frame) was used to record calcium activity in ChP explants or *in vivo* from mice expressing GCaMP6f in epithelial cells (in *FoxJ1-Cre::Ai95D mice*). Imaging and analyses were performed as described[14] with a 25X magnification, 8 mm working distance objective. Laser power measured below the objective at 940 nm was 50–60 mW, using a Mai Tai DeepSee laser (Spectra-Physics). Plasma (using citrate as anti-coagulant instead of EDTA, same protocol as described above) was delivered to explants by topical application from a glass capillary needle and serum was delivered to the lateral ventricle of live mice during imaging through the injection cannula. Serum was prepared by collecting blood using the same approach as described above, incubating on ice for 30 minutes and then centrifuging for 10 minutes at 5,000 g twice to separate the supernatant. For infusions via microinjection cannulas during *in vivo* two-photon imaging, approximately 30 μl aCSF or serum was delivered by syringe pump at a rate of 5 μL / min. Chemicals used on explants include: LiCl (30 mM x15 min), BAPTA-AM (5 mM), 2-APB (50 μM), EGTA (0.5 mM), and EDTA (by collecting blood into EDTA-coated tubes; Cat# BD 365974).

ICV injections—Timed pregnant mice (E14.5) were anesthetized with isoflurane and kept warm. Following laparotomy, AAV solution or age-matched whole blood was delivered into the lateral ventricle of each embryo (located visually) with glass capillary pipettes at rate of 0.5 – 1 μl / s. Due to the time constraints of blood clotting inside the glass capillary pipettes, the total time for donor acquisition and recipient injection of whole blood into each embryo was 15–30 seconds. The uterine horns were returned to the abdomen and the incisions sutured. P4 pups were anesthetized by hypothermia and adults by isoflurane. An incision was made along the midline of the scalp to expose the skull and a 26G needle (pups) or hand drill (adults) was used to pierce the skull directly above the lateral ventricle. AAV solution or age-matched whole blood was delivered into the lateral ventricle through the piercing using glass capillary pipettes. Skin incisions were closed with suture and Vetbond (3M).

Potassium and osmolarity measurements—Potassium in 5–7 μl of mouse CSF and 10–20 μl of human CSF was measured by inductively coupled plasma - optical emission spectrometry (ICP-OES) by Galbraith Laboratories, Inc (Knoxville, TN, USA). Osmolarity of CSF samples was measured with a Wescor VAPRO vapor pressure osmometer. In mouse studies, 5 μl of CSF was first diluted with 10 μl ddH2O. 10 μl of the diluted sample was loaded to the osmometer, ddH2O was used to determine blank value, and the osmolarity of CSF was calculated by (sample value – ddH2O value) in triplicate. 10 μl human CSF was used without dilution.

Blood cell lysis—CSF was collected from adult mice as described above. Whole blood or purified red blood cells were collected from the same donors by cardiac puncture with a 22G needle. To purify red blood cells, 500 µl of whole blood was mixed with 50 µl 3.2% sodium citrate and centrifuged at 500g x 10 minutes at 4°C. Following washes with 1ml sterile PBS in triplicate, samples were resuspended in 500 µl sterile PBS. 5 µl whole blood or purified red blood cells were mixed with 10 µl CSF, allowed to settle, and then incubated at 37°C with images taken at the start and after 24 and 48 hours of incubation.

Immunohistochemistry—Postnatal animals were perfused with phosphate-buffered saline (PBS) followed by 4% paraformaldehyde (PFA). The brains were quickly dissected and post-fixed with 4% PFA overnight. Samples were cryoprotected and prepared for embedding at 4°C with 10% sucrose, 20% sucrose, 30% sucrose, 1:1 mixture of 30% sucrose and OCT (overnight), and OCT (1 hour on ice). Samples were frozen in OCT. Cryosections were blocked and permeabilized (0.3% Triton-X-100 in PBS; 5% goat serum), incubated in primary antibodies at 4°C overnight and secondary antibodies for 2 hours at room temperature. Hoechst 33342 (Invitrogen H3570, 1:10000, 5 minutes at room temperature) was used to visualize nuclei. Sections were mounted using Fluoromount-G (SouthernBiotech). Images were acquired using Zeiss LSM880 confocal microscope with 20x objective. ZEN Black software was used for image acquisition and ZEN Blue used for Airy processing.

Immunoblotting—Tissues were quickly dissected in cold HBSS and homogenized in RIPA buffer supplemented with protease and phosphatase inhibitors. The homogenate was centrifuged at maximum speed for 10 minutes to remove cellular debris. Protein concentration was determined by BCA assay (Thermo Scientific #23227). Samples were denatured in 2% SDS supplemented with 2-Mercaptoethanol by heating at 37°C for 5 minutes. Equal amounts of proteins were loaded and separated by electrophoresis in a 4–15% gradient polyacrylamide gel (BioRad #1653320) or NuPAGE 4–12% Bis-Tris gel (Invitrogen #NP0322), transferred to a nitrocellulose membrane (250 mA, 1.5 hours, on ice), blocked in filtered 5% milk in TBST, incubated with primary antibodies overnight at 4°C followed by HRP conjugated secondary antibodies (1:5,000) for 1 hour, and visualized with ECL substrate. For phosphorylated protein analysis, the phospho-proteins were probed first, and then blots were stripped (Thermo Scientific #21059) and re-probed for total proteins. Band intensity was quantified by FIJI.

MRI and CT imaging—Isoflurane anesthetized mice were kept warm with a heating pad. MRIs were obtained with a Bruker BioSpec small animal MRI (7T); T2 image criteria: TE/TR = 60/4000; Ave = 4; RARE = 4; slice thickness = 0.6 mm. CTs were obtained with the Bruker Albira microCT scanner (45 kV, 0.4 mA settings). CT images were analyzed with AMIDE and Slicer software.

Constant aCSF infusion test—Briefly and as previously described,[27] a single catheter coupled with an ICP sensor was implanted into the lateral ventricle of an anesthetized mouse. A syringe pump was used to infuse aCSF through the catheter at a constant rate (4 µL / min) while ICP was simultaneously measured. The Marmarou model of CSF dynamics

for constant rate infusions were used to calculate parameters describing CSF dynamics by a non-linear least squares fit of the model to the ICP data.[83] The intracranial compliance coefficient (mL) is the reciprocal of Marmarou's intracranial elasticity coefficient (mL^{-1}). CSF conductance ((mL / min) / mmHg) is the reciprocal of Marmarou's resistance to CSF reabsorption/outflow (mmHg / (mL / min)). The coefficients were normalized to the average PBS control value on each acquisition date.

AAVs—Production and purification were performed by University of Pennsylvania (Penn) Vector Core (for AAV-NKCC1: hNKCC1 with CMV promoter, modified from Addgene plasmid # 49077; for AAV-NKCC1_NT51: hNKCC1 with N-terminal mutation to prevent phosphorylation, modified from Addgene plasmid #49061 with the same approach as with AAV-NKCC1)[27] or BCH Viral Core (for AAV-GFP).

QUANTIFICATION AND STATISTICAL ANALYSIS

Statistics—Animal sex, housing, and disease severity were randomized. Biological replicates (N) were defined as samples from distinct individuals except where it was necessary to pooled samples across multiple individuals to obtain sufficient material to make a measurement. All data were collected from at least 2 independent experiments conducted on different dates, with the same protocols. Sample sizes were informed by estimated mean values from preliminary data and previous studies. At least 4 animals from different litters/cohorts were used for each study. Data analyses were performed in a blinded manner whenever possible. For the blood proteome study, the list of proteins was processed in Perseus 1.6.0, log2-transformed, and proteins with fewer than two peptides (razor) were excluded.[79] Principal component analysis was performed on the samples by an unsupervised hierarchical clustering-based heat map. A pairwise comparison was realized on each age group, the results depicted with a Volcano plot, and a permutation-based FDR testing correction was applied for the significant proteins. Other statistical analyses were performed with Prism 7. Statistics were calculated and are presented both with and without outliers identified by the ROUT method (Q = 1%). Appropriate statistical tests were selected based on the distribution of data, homogeneity of variances, and sample sizes. Most of the analyses were performed using One-way ANOVA or Welch's unpaired t-test. F tests or Bartlett's tests were used to assess homogeneity of variances between data sets. Parametric tests (t-test, ANOVA) were used only if data were normally distributed, and variances were approximately equal. Otherwise, nonparametric alternatives were chosen. Data are presented as mean ± standard deviation (SD). See figure legends for statistical tests and sample sizes for each experiment. p values < 0.05 were considered significant (*p <0.05, ** p <0.01, *** p <0.001, **** p <0.0001).

Supplementary Material

Refer to Web version on PubMed Central for supplementary material.

ACKNOWLEDGEMENTS

We thank the Lehtinen, Andermann, and Warf labs for helpful discussions; Kai Kaila and Biff Forbush for discussions relating to NKCC1; Nancy Chamberlin for critical reading and editing of the manuscript; Chinfei Chen and BCH IDDRC Cellular Imaging Core; Janelle Lestrade, Yaotang Wu, Michael Marcotrigiano, Kristina

Pelkola, and BCH Small Animal Imaging Laboratory; BCH viral core; University of Pennsylvania Vector Core. This work was supported by: William Randolph Hearst Fund (H.X.); NIH T32 HL110852 and OFD/BTREC/CTREC Faculty Development Fellowship Award (R.M.F. & N.D.); Harvard College Research Program (M.T.); NIH T32 HL007901 and F30 DK131642 (P.N.K.); T32 GM007753 and T32 GM144273 (P.N.K. & M.E.Z.); American Heart Association Pre-doctoral Fellowship (M.E.Z.) and Little Giraffe Foundation (M.E.Z. & M.K.L.); NSF Graduate Research Fellowship Program (F.B.S.); Reagan Sloane Shanley Research Internship (N.D.); NIH F31 NS115369 (E.M.K.); NIH R01 AI130591 and R35 HL145242 (M.J.H.); NeuroNex/NSF 1707352 and Korn family gift (C.I.M.); NIH R00 HD083512 (P-Y.L.) and R01 HD096693 (P-Y.L. & B.C.W.); NIH U24 AI152179 (H.S.); NIH DP1 AT010971 (M.L.A.); Hydrocephalus Association Discovery Science Award, Pediatric Hydrocephalus Foundation, Human Frontier Science Program #RGP0063/2018 (M.K.L.), Pappendick Family Therapeutic Acceleration Award and the Translational Research Program, NIH R01 NS088566, NS129823, New York Stem Cell Foundation (M.K.L.); NIH RF1 DA048790 (M.K.L. & C.I.M.); BCH IDDRC 1U54HD090255, BCH viral core P30EY012196. The content is solely the responsibility of the authors and does not necessarily represent the official views of the National Institute of General Medical Sciences or NIH.

REFERENCES

1. Kulkarni AV, Riva-Cambrin J, Butler J, Browd SR, Drake JM, Holubkov R, Kestle JR, Limbrick DD, Simon TD, Tamber MS, et al. (2013). Outcomes of CSF shunting in children: comparison of Hydrocephalus Clinical Research Network cohort with historical controls: clinical article. J Neurosurg Pediatr 12, 334–338. 10.3171/2013.7.PEDS12637. [PubMed: 23909616]
2. Robinson S (2012). Neonatal posthemorrhagic hydrocephalus from prematurity: pathophysiology and current treatment concepts. J Neurosurg Pediatr 9, 242–258. 10.3171/2011.12.PEDS11136. [PubMed: 22380952]
3. Kahle KT, Kulkarni AV, Limbrick DD Jr., and Warf BC (2016). Hydrocephalus in children. Lancet 387, 788–799. 10.1016/S0140-6736(15)60694-8. [PubMed: 26256071]
4. Warf BC (2005). Comparison of endoscopic third ventriculostomy alone and combined with choroid plexus cauterization in infants younger than 1 year of age: a prospective study in 550 African children. J Neurosurg 103, 475–481. 10.3171/ped.2005.103.6.0475. [PubMed: 16383244]
5. Kulkarni AV, Schiff SJ, Mbabazi-Kabachelor E, Mugamba J, Ssenyonga P, Donnelly R, Levenbach J, Monga V, Peterson M, MacDonald M, et al. (2017). Endoscopic Treatment versus Shunting for Infant Hydrocephalus in Uganda. N Engl J Med 377, 2456–2464. 10.1056/NEJMoa1707568. [PubMed: 29262276]
6. Chung DY, Thompson BB, Kumar MA, Mahta A, Rao SS, Lai JH, Tadevosyan A, Kessler K, Locascio JJ, Patel AB, et al. (2022). Association of External Ventricular Drain Wean Strategy with Shunt Placement and Length of Stay in Subarachnoid Hemorrhage: A Prospective Multicenter Study. Neurocrit Care 36, 536–545. 10.1007/s12028-021-01343-9. [PubMed: 34498207]
7. Cizmeci MN, Groenendaal F, Liem KD, van Haastert IC, Benavente-Fernandez I, van Straaten HLM, Steggerda S, Smit BJ, Whitelaw A, Woerdeman P, et al. (2020). Randomized Controlled Early versus Late Ventricular Intervention Study in Posthemorrhagic Ventricular Dilatation: Outcome at 2 Years. J Pediatr 226, 28–35 e23. 10.1016/j.jpeds.2020.08.014. [PubMed: 32800815]
8. Simon TD, Riva-Cambrin J, Srivastava R, Bratton SL, Dean JM, Kestle JR, and Hydrocephalus Clinical Research N (2008). Hospital care for children with hydrocephalus in the United States: utilization, charges, comorbidities, and deaths. J Neurosurg Pediatr 1, 131–137. 10.3171/PED/2008/1/2/131. [PubMed: 18352782]
9. Maitre NL, Marshall DD, Price WA, Slaughter JC, O'Shea TM, Maxfield C, and Goldstein RF (2009). Neurodevelopmental outcome of infants with unilateral or bilateral periventricular hemorrhagic infarction. Pediatrics 124, e1153–1160. 10.1542/peds.2009-0953. [PubMed: 19948617]
10. Ballabh P, and de Vries LS (2021). White matter injury in infants with intraventricular haemorrhage: mechanisms and therapies. Nat Rev Neurol 17, 199–214. 10.1038/s41582-020-00447-8. [PubMed: 33504979]
11. Spector R, Keep RF, Robert Snodgrass S, Smith QR, and Johanson CE (2015). A balanced view of choroid plexus structure and function: Focus on adult humans. Exp Neurol 267, 78–86. 10.1016/j.expneurol.2015.02.032. [PubMed: 25747036]
12. Pardridge WM (2016). CSF, blood-brain barrier, and brain drug delivery. Expert Opin Drug Deliv 13, 963–975. 10.1517/17425247.2016.1171315. [PubMed: 27020469]

13. Praetorius J, and Damkier HH (2017). Transport across the choroid plexus epithelium. Am J Physiol Cell Physiol 312, C673–C686. 10.1152/ajpcell.00041.2017. [PubMed: 28330845]

14. Shipley FB, Dani N, Xu H, Deister C, Cui J, Head JP, Sadegh C, Fame RM, Shannon ML, Flores VI, et al. (2020). Tracking Calcium Dynamics and Immune Surveillance at the Choroid Plexus Blood-Cerebrospinal Fluid Interface. Neuron 108, 623–639 e610. 10.1016/j.neuron.2020.08.024. [PubMed: 32961128]

15. Damkier HH, Brown PD, and Praetorius J (2013). Cerebrospinal fluid secretion by the choroid plexus. Physiol Rev 93, 1847–1892. 10.1152/physrev.00004.2013. [PubMed: 24137023]

16. Fame RM, and Lehtinen MK (2020). Emergence and Developmental Roles of the Cerebrospinal Fluid System. Dev Cell 52, 261–275. 10.1016/j.devcel.2020.01.027. [PubMed: 32049038]

17. Haddad MR, Donsante A, Zerfas P, and Kaler SG (2013). Fetal Brain-directed AAV Gene Therapy Results in Rapid, Robust, and Persistent Transduction of Mouse Choroid Plexus Epithelia. Mol Ther Nucleic Acids 2, e101. 10.1038/mtna.2013.27. [PubMed: 23799375]

18. Cui J, Shipley FB, Shannon ML, Alturkistani O, Dani N, Webb MD, Sugden AU, Andermann ML, and Lehtinen MK (2020). Inflammation of the Embryonic Choroid Plexus Barrier following Maternal Immune Activation. Dev Cell 55, 617–628 e616. 10.1016/j.devcel.2020.09.020. [PubMed: 33038331]

19. Jang A, and Lehtinen MK (2022). Experimental approaches for manipulating choroid plexus epithelial cells. Fluids Barriers CNS 26*;19(1):*36. 10.1186/s12987-022-00330-2.

20. Liu G, Martins I, Wemmie JA, Chiorini JA, and Davidson BL (2005). Functional correction of CNS phenotypes in a lysosomal storage disease model using adeno-associated virus type 4 vectors. J Neurosci 25, 9321–9327. 10.1523/JNEUROSCI.2936-05.2005. [PubMed: 16221840]

21. Hudry E, Dashkoff J, Roe AD, Takeda S, Koffie RM, Hashimoto T, Scheel M, Spires-Jones T, Arbel-Ornath M, Betensky R, et al. (2013). Gene transfer of human Apoe isoforms results in differential modulation of amyloid deposition and neurotoxicity in mouse brain. Sci Transl Med 5, 212ra161. 10.1126/scitranslmed.3007000.

22. Benraiss A, Toner MJ, Xu Q, Bruel-Jungerman E, Rogers EH, Wang F, Economides AN, Davidson BL, Kageyama R, Nedergaard M, and Goldman SA (2013). Sustained mobilization of endogenous neural progenitors delays disease progression in a transgenic model of Huntington's disease. Cell Stem Cell 12, 787–799. 10.1016/j.stem.2013.04.014. [PubMed: 23746982]

23. Jang A, Petrova B, Cheong TC, Zawadzki ME, Jones JK, Culhane AJ, Shipley FB, Chiarle R, Wong ET, Kanarek N, and Lehtinen MK (2022). Choroid plexus-CSF-targeted antioxidant therapy protects the brain from toxicity of cancer chemotherapy. Neuron 110, 3288–3301 e3288. 10.1016/j.neuron.2022.08.009. [PubMed: 36070751]

24. Simard PF, Tosun C, Melnichenko L, Ivanova S, Gerzanich V, and Simard JM (2011). Inflammation of the choroid plexus and ependymal layer of the ventricle following intraventricular hemorrhage. Transl Stroke Res 2, 227–231. 10.1007/s12975-011-0070-8. [PubMed: 21731590]

25. Karimy JK, Zhang J, Kurland DB, Theriault BC, Duran D, Stokum JA, Furey CG, Zhou X, Mansuri MS, Montejo J, et al. (2017). Inflammation-dependent cerebrospinal fluid hypersecretion by the choroid plexus epithelium in posthemorrhagic hydrocephalus. Nat Med 23, 997–1003. 10.1038/nm.4361. [PubMed: 28692063]

26. Delpire E, and Gagnon KB (2019). Elusive role of the Na-K-2Cl cotransporter in the choroid plexus. Am J Physiol Cell Physiol 316, C522–C524. 10.1152/ajpcell.00490.2018. [PubMed: 30576234]

27. Xu H, Fame RM, Sadegh C, Sutin J, Naranjo C, Della S, Cui J, Shipley FB, Vernon A, Gao F, et al. (2021). Choroid plexus NKCC1 mediates cerebrospinal fluid clearance during mouse early postnatal development. Nat Commun 12, 447. 10.1038/s41467-020-20666-3. [PubMed: 33469018]

28. Gregoriades JMC, Madaris A, Alvarez FJ, and Alvarez-Leefmans FJ (2019). Genetic and pharmacological inactivation of apical Na(+)-K(+)-2Cl(−) cotransporter 1 in choroid plexus epithelial cells reveals the physiological function of the cotransporter. Am J Physiol Cell Physiol 316, C525–C544. 10.1152/ajpcell.00026.2018. [PubMed: 30576237]

29. Milhorat TH, Mosher MB, Hammock MK, and Murphy CF (1970). Evidence for choroid-plexus absorption in hydrocephalus. N Engl J Med 283, 286–289. 10.1056/NEJM197008062830604. [PubMed: 5427058]

30. Oreskovic D, Rados M, and Klarica M (2017). Role of choroid plexus in cerebrospinal fluid hydrodynamics. Neuroscience 354, 69–87. 10.1016/j.neuroscience.2017.04.025. [PubMed: 28456718]

31. Wu Q, Delpire E, Hebert SC, and Strange K (1998). Functional demonstration of Na+-K+−2Cl- cotransporter activity in isolated, polarized choroid plexus cells. Am J Physiol 275, C1565–1572. 10.1152/ajpcell.1998.275.6.C1565. [PubMed: 9843718]

32. Darman RB, and Forbush B (2002). A regulatory locus of phosphorylation in the N terminus of the Na-K-Cl cotransporter, NKCC1. J Biol Chem 277, 37542–37550. 10.1074/jbc.M206293200. [PubMed: 12145304]

33. Strahle J, Garton HJ, Maher CO, Muraszko KM, Keep RF, and Xi G (2012). Mechanisms of hydrocephalus after neonatal and adult intraventricular hemorrhage. Transl Stroke Res 3, 25–38. 10.1007/s12975-012-0182-9. [PubMed: 23976902]

34. Robinson S, Conteh FS, Oppong AY, Yellowhair TR, Newville JC, Demerdash NE, Shrock CL, Maxwell JR, Jett S, Northington FJ, and Jantzie LL (2018). Extended Combined Neonatal Treatment With Erythropoietin Plus Melatonin Prevents Posthemorrhagic Hydrocephalus of Prematurity in Rats. Front Cell Neurosci 12, 322. 10.3389/fncel.2018.00322. [PubMed: 30319361]

35. Yung YC, Mutoh T, Lin ME, Noguchi K, Rivera RR, Choi JW, Kingsbury MA, and Chun J (2011). Lysophosphatidic acid signaling may initiate fetal hydrocephalus. Sci Transl Med 3, 99ra87. 10.1126/scitranslmed.3002095.

36. Workman AD, Charvet CJ, Clancy B, Darlington RB, and Finlay BL (2013). Modeling transformations of neurodevelopmental sequences across mammalian species. J Neurosci 33, 7368–7383. 10.1523/JNEUROSCI.5746-12.2013. [PubMed: 23616543]

37. Tully HM, and Dobyns WB (2014). Infantile hydrocephalus: a review of epidemiology, classification and causes. Eur J Med Genet 57, 359–368. 10.1016/j.ejmg.2014.06.002. [PubMed: 24932902]

38. Tully HM, Ishak GE, Rue TC, Dempsey JC, Browd SR, Millen KJ, Doherty D, and Dobyns WB (2016). Two Hundred Thirty-Six Children With Developmental Hydrocephalus: Causes and Clinical Consequences. J Child Neurol 31, 309–320. 10.1177/0883073815592222. [PubMed: 26184484]

39. Papile LA, Burstein J, Burstein R, and Koffler H (1978). Incidence and evolution of subependymal and intraventricular hemorrhage: a study of infants with birth weights less than 1,500 gm. J Pediatr 92, 529–534. 10.1016/s0022-3476(78)80282-0. [PubMed: 305471]

40. Dias SF, Lalou AD, Spang R, Haas-Lude K, Garnett M, Fernandez H, Czosnyka M, Schuhmann MU, and Czosnyka Z (2020). Value of computerized shunt infusion study in assessment of pediatric hydrocephalus shunt function-a two center cross-sectional study. Childs Nerv Syst 36, 59–71. 10.1007/s00381-019-04264-3. [PubMed: 31372736]

41. Eide PK, and Brean A (2010). Cerebrospinal fluid pulse pressure amplitude during lumbar infusion in idiopathic normal pressure hydrocephalus can predict response to shunting. Cerebrospinal Fluid Res 7, 5. 10.1186/1743-8454-7-5. [PubMed: 20205911]

42. Aquilina K, Pople IK, Sacree J, Carter MR, and Edwards RJ (2012). The constant flow ventricular infusion test: a simple and useful study in the diagnosis of third ventriculostomy failure. J Neurosurg 116, 445–452. 10.3171/2011.10.JNS1140. [PubMed: 22098198]

43. Eide PK (2018). The pathophysiology of chronic noncommunicating hydrocephalus: lessons from continuous intracranial pressure monitoring and ventricular infusion testing. J Neurosurg 129, 220–233. 10.3171/2017.1.JNS162813. [PubMed: 28799879]

44. Lopes Lda S, Slobodian I, and Del Bigio MR (2009). Characterization of juvenile and young adult mice following induction of hydrocephalus with kaolin. Exp Neurol 219, 187–196. 10.1016/j.expneurol.2009.05.015. [PubMed: 19460371]

45. Li Q, Aalling NN, Forstera B, Erturk A, Nedergaard M, Mollgard K, and Xavier ALR (2020). Aquaporin 1 and the Na(+)/K(+)/2Cl(−) cotransporter 1 are present in the leptomeningeal vasculature of the adult rodent central nervous system. Fluids Barriers CNS 17, 15. 10.1186/s12987-020-0176-z. [PubMed: 32046744]

46. Karimy JK, Duran D, Hu JK, Gavankar C, Gaillard JR, Bayri Y, Rice H, DiLuna ML, Gerzanich V, Marc Simard J, and Kahle KT (2016). Cerebrospinal fluid hypersecretion in pediatric hydrocephalus. Neurosurg Focus 41, E10. 10.3171/2016.8.FOCUS16278.
47. Mazucanti CH, Liu QR, Lang D, Huang N, O'Connell JF, Camandola S, and Egan JM (2019). Release of insulin produced by the choroid plexis is regulated by serotonergic signaling. JCI Insight 4. 10.1172/jci.insight.131682.
48. Zhang S, Zhou J, Zhang Y, Liu T, Friedel P, Zhuo W, Somasekharan S, Roy K, Zhang L, Liu Y, et al. (2021). The structural basis of function and regulation of neuronal cotransporters NKCC1 and KCC2. Commun Biol 4, 226. 10.1038/s42003-021-01750-w. [PubMed: 33597714]
49. Loscher W, and Kaila K (2022). CNS pharmacology of NKCC1 inhibitors. Neuropharmacology 205, 108910. 10.1016/j.neuropharm.2021.108910. [PubMed: 34883135]
50. Berridge MJ, Downes CP, and Hanley MR (1989). Neural and developmental actions of lithium: a unifying hypothesis. Cell 59, 411–419. 10.1016/0092-8674(89)90026-3. [PubMed: 2553271]
51. Maruyama T, Kanaji T, Nakade S, Kanno T, and Mikoshiba K (1997). 2APB, 2-aminoethoxydiphenyl borate, a membrane-penetrable modulator of Ins(1,4,5)P3-induced Ca2+ release. J Biochem 122, 498–505. 10.1093/oxfordjournals.jbchem.a021780. [PubMed: 9348075]
52. Pisanu C, Melis C, and Squassina A (2016). Lithium Pharmacogenetics: Where Do We Stand? Drug Dev Res 77, 368–373. 10.1002/ddr.21341. [PubMed: 27633500]
53. Hirsch ML, Wolf SJ, and Samulski RJ (2016). Delivering Transgenic DNA Exceeding the Carrying Capacity of AAV Vectors. Methods Mol Biol 1382, 21–39. 10.1007/978-1-4939-3271-9_2. [PubMed: 26611576]
54. Somasekharan S, Monette MY, and Forbush B (2013). Functional expression of human NKCC1 from a synthetic cassette-based cDNA: introduction of extracellular epitope tags and removal of cysteines. PLoS One 8, e82060. 10.1371/journal.pone.0082060. [PubMed: 24339991]
55. Stapleton CJ, Acharjee A, Irvine HJ, Wolcott ZC, Patel AB, and Kimberly WT (2019). High-throughput metabolite profiling: identification of plasma taurine as a potential biomarker of functional outcome after aneurysmal subarachnoid hemorrhage. J Neurosurg, 1–8. 10.3171/2019.9.JNS191346.
56. Koch M, Acharjee A, Ament Z, Schleicher R, Bevers M, Stapleton C, Patel A, and Kimberly WT (2021). Machine Learning-Driven Metabolomic Evaluation of Cerebrospinal Fluid: Insights Into Poor Outcomes After Aneurysmal Subarachnoid Hemorrhage. Neurosurgery 88, 1003–1011. 10.1093/neuros/nyaa557. [PubMed: 33469656]
57. Wilson CD, Safavi-Abbasi S, Sun H, Kalani MY, Zhao YD, Levitt MR, Hanel RA, Sauvageau E, Mapstone TB, Albuquerque FC, et al. (2017). Meta-analysis and systematic review of risk factors for shunt dependency after aneurysmal subarachnoid hemorrhage. J Neurosurg 126, 586–595. 10.3171/2015.11.JNS152094. [PubMed: 27035169]
58. Russell JM (2000). Sodium-potassium-chloride cotransport. Physiol Rev 80, 211–276. 10.1152/physrev.2000.80.1.211. [PubMed: 10617769]
59. Stutchfield PR, and Cooke RW (1989). Electrolytes and glucose in cerebrospinal fluid of premature infants with intraventricular haemorrhage: role of potassium in cerebral infarction. Arch Dis Child 64, 470–475. 10.1136/adc.64.4_spec_no.470. [PubMed: 2730115]
60. Kurki SN, Uvarov P, Pospelov AS, Trontti K, Hubner AK, Srinivasan R, Watanabe M, Hovatta I, Hubner CA, Kaila K, and Virtanen MA (2022). Expression patterns of NKCC1 in neurons and non-neuronal cells during cortico-hippocampal development. Cereb Cortex. 10.1093/cercor/bhac470.
61. Koumangoye R, Bastarache L, and Delpire E (2021). NKCC1: Newly Found as a Human Disease-Causing Ion Transporter. Function (Oxf) 2, zqaa028. 10.1093/function/zqaa028. [PubMed: 33345190]
62. Trifan G, Arshi B, and Testai FD (2019). Intraventricular Hemorrhage Severity as a Predictor of Outcome in Intracerebral Hemorrhage. Front Neurol 10, 217. 10.3389/fneur.2019.00217. [PubMed: 30915027]
63. Behrens P, Tietze A, Walch E, Bittigau P, Buhrer C, Schulz M, Aigner A, and Thomale UW (2020). Neurodevelopmental outcome at 2 years after neuroendoscopic lavage in neonates with

posthemorrhagic hydrocephalus. J Neurosurg Pediatr 26, 495–503. 10.3171/2020.5.PEDS20211. [PubMed: 32764179]

64. Luyt K, Jary SL, Lea CL, Young GJ, Odd DE, Miller HE, Kmita G, Williams C, Blair PS, Hollingworth W, et al. (2020). Drainage, irrigation and fibrinolytic therapy (DRIFT) for posthaemorrhagic ventricular dilatation: 10-year follow-up of a randomised controlled trial. Arch Dis Child Fetal Neonatal Ed 105, 466–473. 10.1136/archdischild-2019-318231. [PubMed: 32623370]
65. Bauer DF, Baird LC, Klimo P, Mazzola CA, Nikas DC, Tamber MS, and Flannery AM (2020). Congress of Neurological Surgeons Systematic Review and Evidence-Based Guidelines on the Treatment of Pediatric Hydrocephalus: Update of the 2014 Guidelines. Neurosurgery 87, 1071–1075. 10.1093/neuros/nyaa434. [PubMed: 34791462]
66. Limbrick DD Jr., and de Vries LS (2022). New insights into the management of post-hemorrhagic hydrocephalus. Semin Perinatol, 151597. 10.1016/j.semperi.2022.151597. [PubMed: 35461702]
67. Proulx ST (2021). Cerebrospinal fluid outflow: a review of the historical and contemporary evidence for arachnoid villi, perineural routes, and dural lymphatics. Cell Mol Life Sci 78, 2429–2457. 10.1007/s00018-020-03706-5. [PubMed: 33427948]
68. Chen J, Wang L, Xu H, Xing L, Zhuang Z, Zheng Y, Li X, Wang C, Chen S, Guo Z, et al. (2020). Meningeal lymphatics clear erythrocytes that arise from subarachnoid hemorrhage. Nat Commun 11, 3159. 10.1038/s41467-020-16851-z. [PubMed: 32572022]
69. Antila S, Karaman S, Nurmi H, Airavaara M, Voutilainen MH, Mathivet T, Chilov D, Li Z, Koppinen T, Park JH, et al. (2017). Development and plasticity of meningeal lymphatic vessels. J Exp Med 214, 3645–3667. 10.1084/jem.20170391. [PubMed: 29141865]
70. Munk AS, Wang W, Bechet NB, Eltanahy AM, Cheng AX, Sigurdsson B, Benraiss A, Mae MA, Kress BT, Kelley DH, et al. (2019). PDGF-B Is Required for Development of the Glymphatic System. Cell Rep 26, 2955–2969 e2953. 10.1016/j.celrep.2019.02.050. [PubMed: 30865886]
71. Riva-Cambrin J, Kestle JRW, Rozzelle CJ, Naftel RP, Alvey JS, Reeder RW, Holubkov R, Browd SR, Cochrane DD, Limbrick DD, et al. (2019). Predictors of success for combined endoscopic third ventriculostomy and choroid plexus cauterization in a North American setting: a Hydrocephalus Clinical Research Network study. J Neurosurg Pediatr 24, 128–138. 10.3171/2019.3.PEDS18532. [PubMed: 31151098]
72. Lehtinen MK, Zappaterra MW, Chen X, Yang YJ, Hill AD, Lun M, Maynard T, Gonzalez D, Kim S, Ye P, et al. (2011). The cerebrospinal fluid provides a proliferative niche for neural progenitor cells. Neuron 69, 893–905. 10.1016/j.neuron.2011.01.023. [PubMed: 21382550]
73. Lun MP, Monuki ES, and Lehtinen MK (2015). Development and functions of the choroid plexus-cerebrospinal fluid system. Nat Rev Neurosci 16, 445–457. 10.1038/nrn3921. [PubMed: 26174708]
74. Akaishi T, Takahashi T, Nakashima I, Abe M, Aoki M, and Ishii T (2020). Osmotic pressure of serum and cerebrospinal fluid in patients with suspected neurological conditions. Neural Regen Res 15, 944–947. 10.4103/1673-5374.268906. [PubMed: 31719261]
75. Perez-Riverol Y, Bai J, Bandla C, Garcia-Seisdedos D, Hewapathirana S, Kamatchinathan S, Kundu DJ, Prakash A, Frericks-Zipper A, Eisenacher M, et al. (2022). The PRIDE database resources in 2022: a hub for mass spectrometry-based proteomics evidences. Nucleic Acids Res 50, D543–D552. 10.1093/nar/gkab1038. [PubMed: 34723319]
76. Zhang Y, Huang G, Shornick LP, Roswit WT, Shipley JM, Brody SL, and Holtzman MJ (2007). A transgenic FOXJ1-Cre system for gene inactivation in ciliated epithelial cells. Am J Respir Cell Mol Biol 36, 515–519. 10.1165/rcmb.2006-0475RC. [PubMed: 17255554]
77. Madisen L, Garner AR, Shimaoka D, Chuong AS, Klapoetke NC, Li L, van der Bourg A, Niino Y, Egolf L, Monetti C, et al. (2015). Transgenic mice for intersectional targeting of neural sensors and effectors with high specificity and performance. Neuron 85, 942–958. 10.1016/j.neuron.2015.02.022. [PubMed: 25741722]
78. Zappaterra MW, LaMantia AS, Walsh CA, and Lehtinen MK (2013). Isolation of cerebrospinal fluid from rodent embryos for use with dissected cerebral cortical explants. J Vis Exp, e50333. 10.3791/50333. [PubMed: 23524481]

79. Tyanova S, Temu T, Sinitcyn P, Carlson A, Hein MY, Geiger T, Mann M, and Cox J (2016). The Perseus computational platform for comprehensive analysis of (prote)omics data. Nat Methods 13, 731–740. 10.1038/nmeth.3901. [PubMed: 27348712]

80. Bennike TB, Bellin MD, Xuan Y, Stensballe A, Moller FT, Beilman GJ, Levy O, Cruz-Monserrate Z, Andersen V, Steen J, et al. (2018). A Cost-Effective High-Throughput Plasma and Serum Proteomics Workflow Enables Mapping of the Molecular Impact of Total Pancreatectomy with Islet Autotransplantation. J Proteome Res 17, 1983–1992. 10.1021/acs.jproteome.8b00111. [PubMed: 29641209]

81. Berger ST, Ahmed S, Muntel J, Cuevas Polo N, Bachur R, Kentsis A, Steen J, and Steen H (2015). MStern Blotting-High Throughput Polyvinylidene Fluoride (PVDF) Membrane-Based Proteomic Sample Preparation for 96-Well Plates. Mol Cell Proteomics 14, 2814–2823. 10.1074/mcp.O115.049650. [PubMed: 26223766]

82. Cox J, and Mann M (2008). MaxQuant enables high peptide identification rates, individualized p.p.b.-range mass accuracies and proteome-wide protein quantification. Nat Biotechnol 26, 1367–1372. 10.1038/nbt.1511. [PubMed: 19029910]

83. Czosnyka M, Czosnyka Z, Agarwal-Harding KJ, and Pickard JD (2012). Modeling of CSF dynamics: legacy of Professor Anthony Marmarou. Acta Neurochir Suppl 113, 9–14. 10.1007/978-3-7091-0923-6_2. [PubMed: 22116414]

84. Schindelin J, Arganda-Carreras I, Frise E, Kaynig V, Longair M, Pietzsch T, Preibisch S, Rueden C, Saalfeld S, Schmid B, Tinevez J-Y, White DJ, Hartenstein V, Eliceiri K, Tomancak P, and Cardona A (2012). Fiji: an open-source platform for biological-image analysis. Nature Methods 9, 676–682. 10.1038/nmeth.2019. [PubMed: 22743772]

Highlights

- CSF-K^+ increases sharply in pediatric and adult post-hemorrhagic hydrocephalus model
- Blood triggers ChP calcium activity and NKCC1 expression / activation
- ChP-NKCC1 overexpression prevents ventriculomegaly and enhances CSF clearance
- Hemorrhagic stroke patient CSF samples revealed dysregulated CSF-K^+ levels

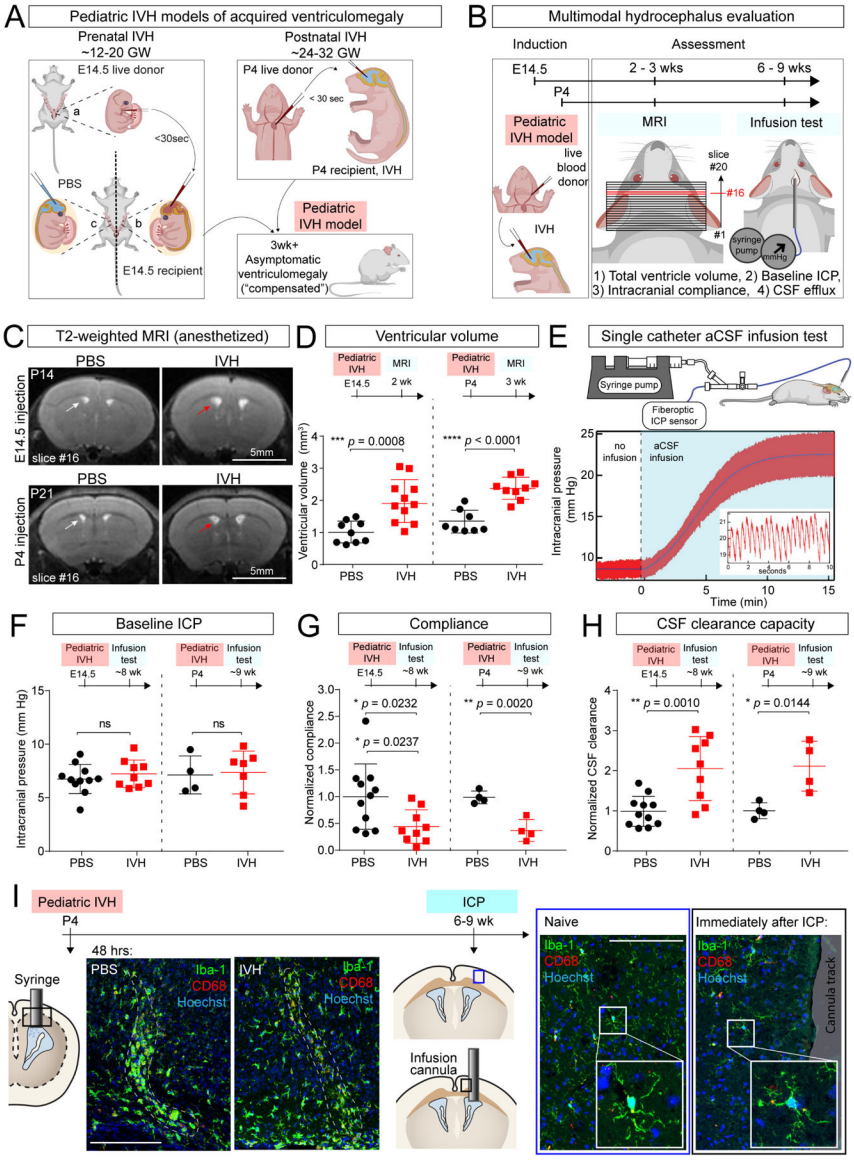

Figure 1. Intraventricular blood leads to ventriculomegaly in mouse models of pediatric PHH.

(**A**) Schematics of IVH models at E14.5 (modeling very preterm human infants of 12–20 gestational weeks (GW)) and at P4 (modeling preterm human infants of 24–32 GW). Age-matched blood from donors (litter a) was obtained and immediately delivered into the lateral ventricles of recipient embryos (litter b). Sterile PBS was used as control (litter c). Similar approach used at P4, where donor, recipients, and PBS controls were littermates. Schematic: grown mice with pediatric IVH have no overt changes in head shape, suggesting *compensated* ventriculomegaly. (**B**) Workflow for IVH induction and hydrocephalus evaluation at E14.5 and P4. (**C**) Representative T2-weighted MRI images (slice #16 of 20-slice series) showing ventriculomegaly in E14.5 and P4 IVH model (red arrow) vs PBS control (white arrow), imaged at P14 and P21, respectively. Scale bar = 5 mm. (**D**) Lateral ventricle volumes in E14.5 and P4 IVH models at P14 and P21, respectively. E14.5: PBS N = 9, IVH N = 11, *** $p = 0.0008$; P4: PBS N = 8, IVH

N = 9, **** $p < 0.0001$. Welch's two-tailed unpaired t-test. Data are mean ± SD. (**E**) Schematic depicting the infusion test and data from an adult control mouse for analysis using the Marmarou model of CSF dynamics. Inset shows representative magnified view of ICP waveforms, which oscillate with the expected frequency of cardiorespiratory pulsations. (**F-H**) Measurements from infusion test, including baseline ICP, compliance, and capacity for CSF clearance. Coefficients of compliance and clearance were normalized with respect to the average PBS control value on each acquisition date. E14.5: PBS N = 11, IVH N = 9; P4: PBS N = 4, IVH N = 4. (F) not significant; (G) * $p = 0.0232$ (if exclude the one outlier, * $p = 0.0237$), ** $p = 0.0020$; (H) * $p = 0.0144$, ** $p = 0.001$. All statistics in F-H were determined by Holm-Sidak method with multiple-comparison corrected. Each data point represents one mouse. (**I**) Activated ($CD68^+$) brain microglia ($Iba1^+$) were restricted to site of needle track 2 days following ICV (dotted lines, left panels). No noticeable microglial activation immediately following ICP infusion through a cannula compared to naïve mice (right panels).

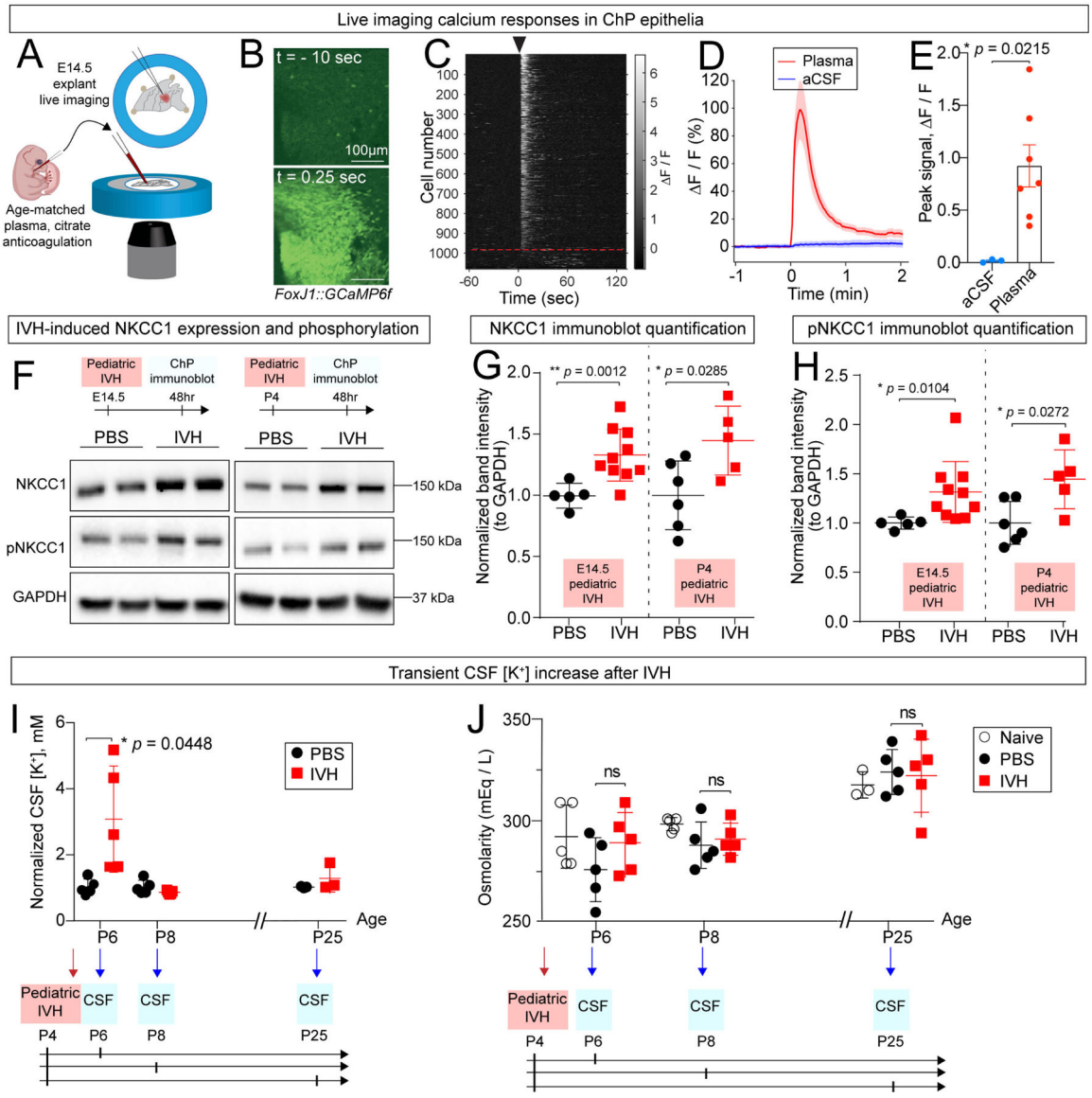

Figure 2. The ChP responds rapidly to ventricular blood exposure.

(**A**) Schematic depicting ChP explant imaging in response to blood exposure. (**B**) Two-photon calcium imaging of ChP explant (*FoxJ1-Cre::GCaMP6f* mice) shows increased response following application of plasma. Scale bar = 100 µm. Top: 10 seconds prior to plasma. Bottom: 0.25 sec after plasma exposure. (**C**) Two-photon calcium activity of epithelial cells shown in (B), sorted by peak activity within 25 seconds following application of plasma. Black arrow indicates onset of plasma. Red dashed line indicates cutoff of non-responder cells (responder cells were defined as those that exceeded the cutoff of 6 standard deviations or more above the pre-stimulation mean within 25 seconds of stimulus exposure), indicating that 91% (987 out of 1080) of ChP epithelial cells are sensitive to plasma. (**D**) Epifluorescence calcium activity of entire ChP explant following addition of plasma (red) and aCSF (blue). Shaded color zones indicate standard deviation (n = 7 mice for plasma, 3 for aCSF). (**E**) ChP calcium activity showing peak intensity. (**F-H**) IVH increased total ChP

NKCC1 and pNKCC1 after 48 hrs. (G) E14.5: PBS N = 5, IVH N = 10, ** $p = 0.0012$; P4: PBS N = 6, IVH N = 5, * $p = 0.02852$. (H) E14.5: PBS N = 5, IVH N = 10, * $p = 0.0104$; P4: PBS N = 6, IVH N = 5, * $p = 0.0272$. Welch's two-tailed unpaired t-test. Data presented as mean ± SD. (**I**) CSF [K^+] increased 2 days after IVH and returned to baseline 4 days after IVH, * $p = 0.0448$. N = 5 for each condition, Welch's two-tailed unpaired t-test. Data presented as mean ± SD. (**J**) CSF osmolarity remained unchanged by IVH. N = 5 for each condition except for uninjected Day 21, where N = 3. Each data point in Figure 2 represents one mouse, except for CSF data where each data point represents one biological replicate, and 2–3 mice were pooled in each biological replicate to reach sufficient CSF volume for performing the assay.

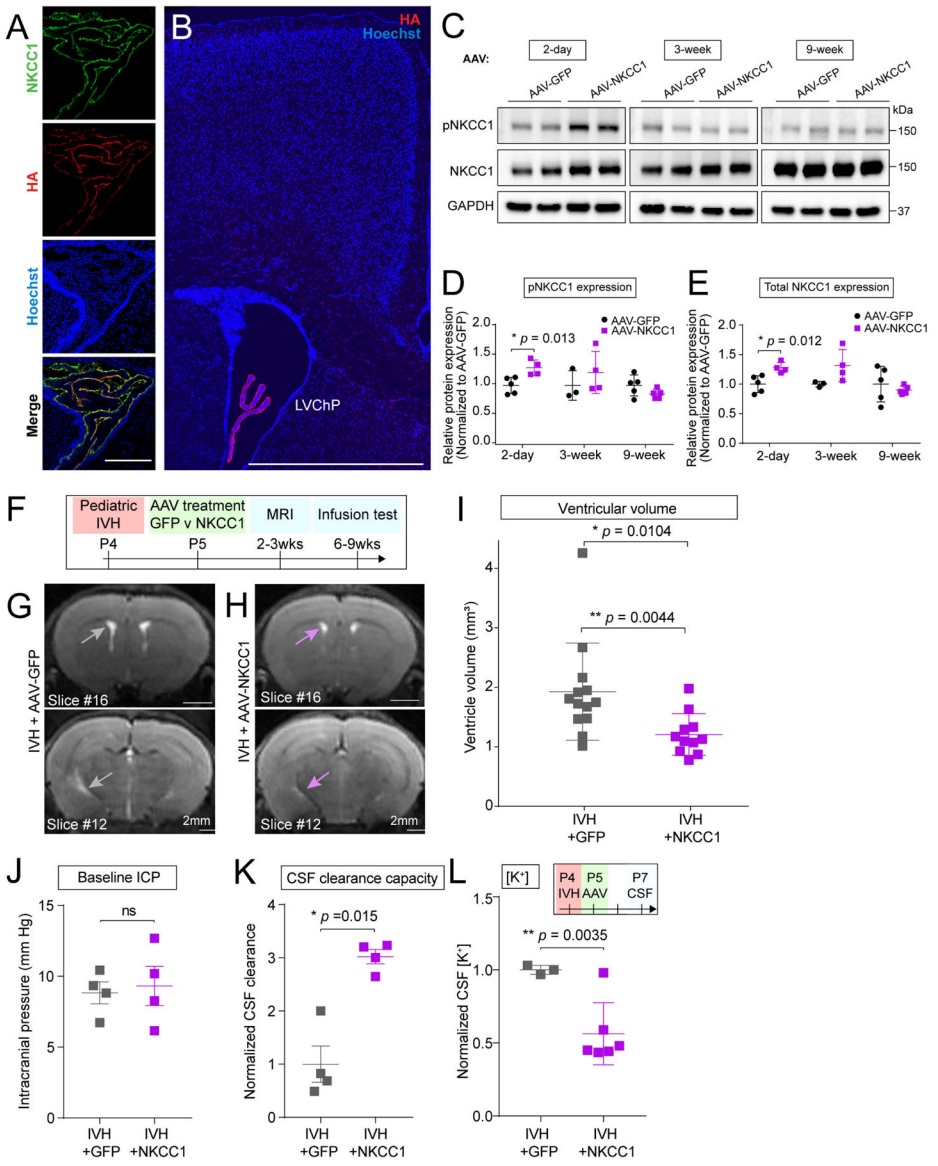

Figure 3. AAV-NKCC1 delivered ICV shows tropism for ChP epithelial cells and mitigates IVH-induced ventriculomegaly in mouse models of pediatric PHH

(**A**) AAV-NKCC1 localizes to apical CSF surface of ChP epithelial cells. Scale = 100 μm. (**B**) HA signal observed in the LV ChP. Scale = 250 μm. (**C-E**) Increased pNKCC1 (quantified in D) and total NKCC1 (quantified in E) levels 2 days following AAV-NKCC1 ICV delivery to P4 pups. NKCC1 overexpression does not persist long term. Welch's two-tailed unpaired t-test. Data presented as mean ± SD. (**F**) Timeline of AAV-NKCC1 treatment following IVH, with AAV-GFP as control. (**G-I**) Representative T2-MRI images and quantification of ventricular volume in IVH mice treated with AAV-GFP (G, grey arrows showing ventricles) vs AAV-NKCC1 (H, light purple arrows showing ventricles). Scale = 2 mm. IVH+GFP N = 13, IVH+NKCC1 N = 11, * $p = 0.0104$ (If exclude the one outlier, * $p = 0.0044$). Welch's two-tailed unpaired t-test. Data presented as mean ± SD. For comparison with values from unpretreated mice, see Fig. 1D. (**J-K**) baseline ICP and capacity for CSF clearance. IVH+GFP N = 4, IVH+NKCC1 N = 4, * $p = 0.015$. Welch's

two-tailed unpaired t-test. Data presented as mean ± SD. (**L**) CSF [K^+] was reduced by AAV-NKCC1 treatment 3 days following IVH. IVH+GFP N = 3, IVH+NKCC1 N = 6, ** $p = 0.0035$. Welch's two-tailed unpaired t-test. Data presented as mean ± SD. Each data point represents one mouse, except for CSF data in Q where each data point represents one biological replicate, and 2–3 mice were pooled in each biological replicate to reach sufficient CSF volume for performing assay.

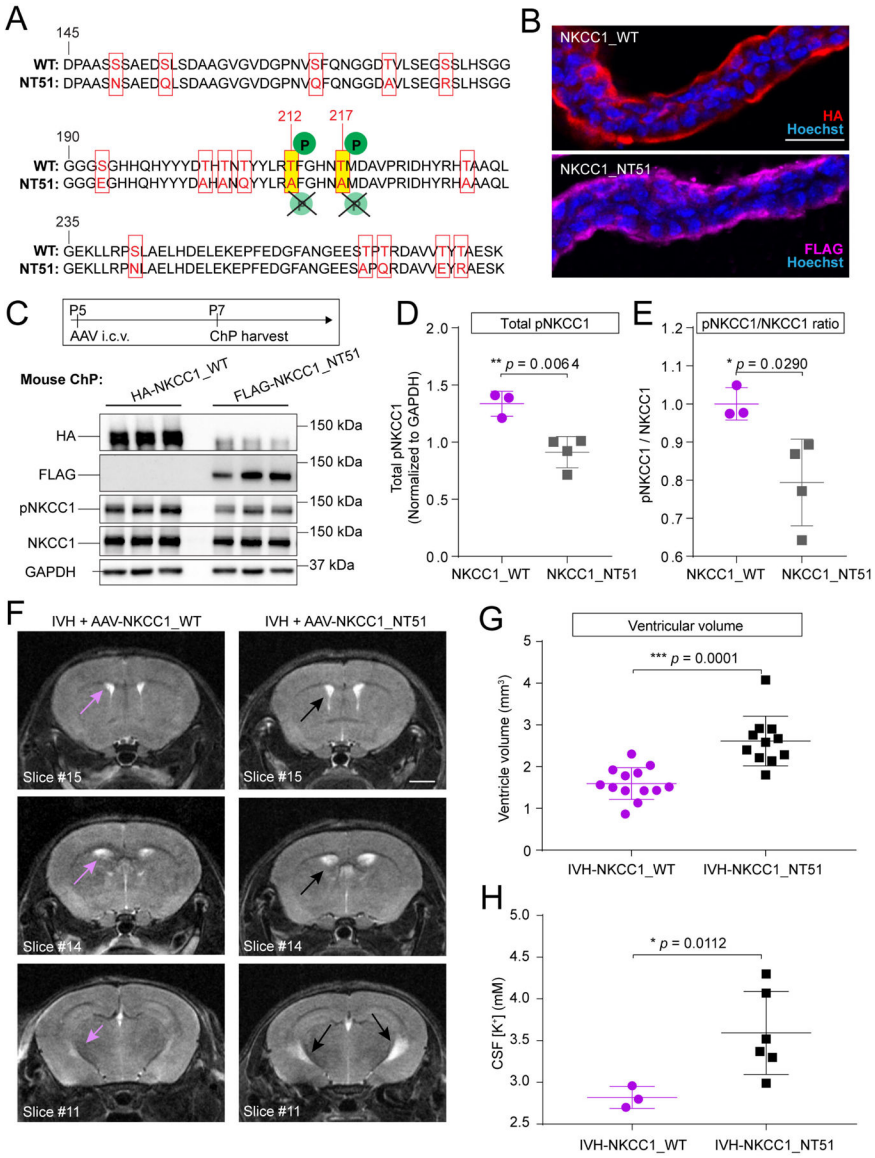

Figure 4. Inactive NKCC1 fails to mitigate ventriculomegaly in IVH mice.

(**A**) Alignment of sequences in the regulatory domain of WT and NKCC1_NT51 shows residues with silent inactivating mutations in NKCC1_NT51. (**B**) ChP apical localization of both WT and NKCC1_NT51, identified by HA and FLAG, respectively. Scale = 25 μm. (**C**) P5 pups expressing AAV-NKCC1_NT51 had lower pNKCC1 level than littermates expressing AAV-NKCC1_WT. (**D-E**) Lower pNKCC1 (D) and lower pNKCC1/NKCC1 ratio (E) by AAV-NKCC1_NT51. AAV-NKCC1_WT N=3, AAV-NKCC1_NT51 N=4. Welch's two-tailed unpaired t-test. Data presented as mean ± SD. (**F-G**) Representative T2-MRI images and quantification of ventricular volume in IVH mice treated with AAV-NKCC1_WT (purple arrows denote ventricles) or AAV-NKCC1_NT51 (black arrows denote ventricles). Scale = 2 mm. IVH+AAV-NKCC1_WT, N = 13; IVH+AAV-NKCC1_NT51 N = 11, *** $p = 0.0001$. Welch's two-tailed unpaired t-test. Data presented as mean ± SD. (**H**) CSF [K^+] was higher in IVH mice treated with AAV-NKCC1-NT51 compared to mice

treated with wild-type AAV-NKCC1 3 days following IVH. Wild-type AAV-NKCC1: N=3 (pooled across 10 pups); AAV-NKCC1-NT51: N=6 (pooled across 16 pups), * $p = 0.0112$. Welch's two-tailed unpaired t-test. Data presented as mean ± SD.

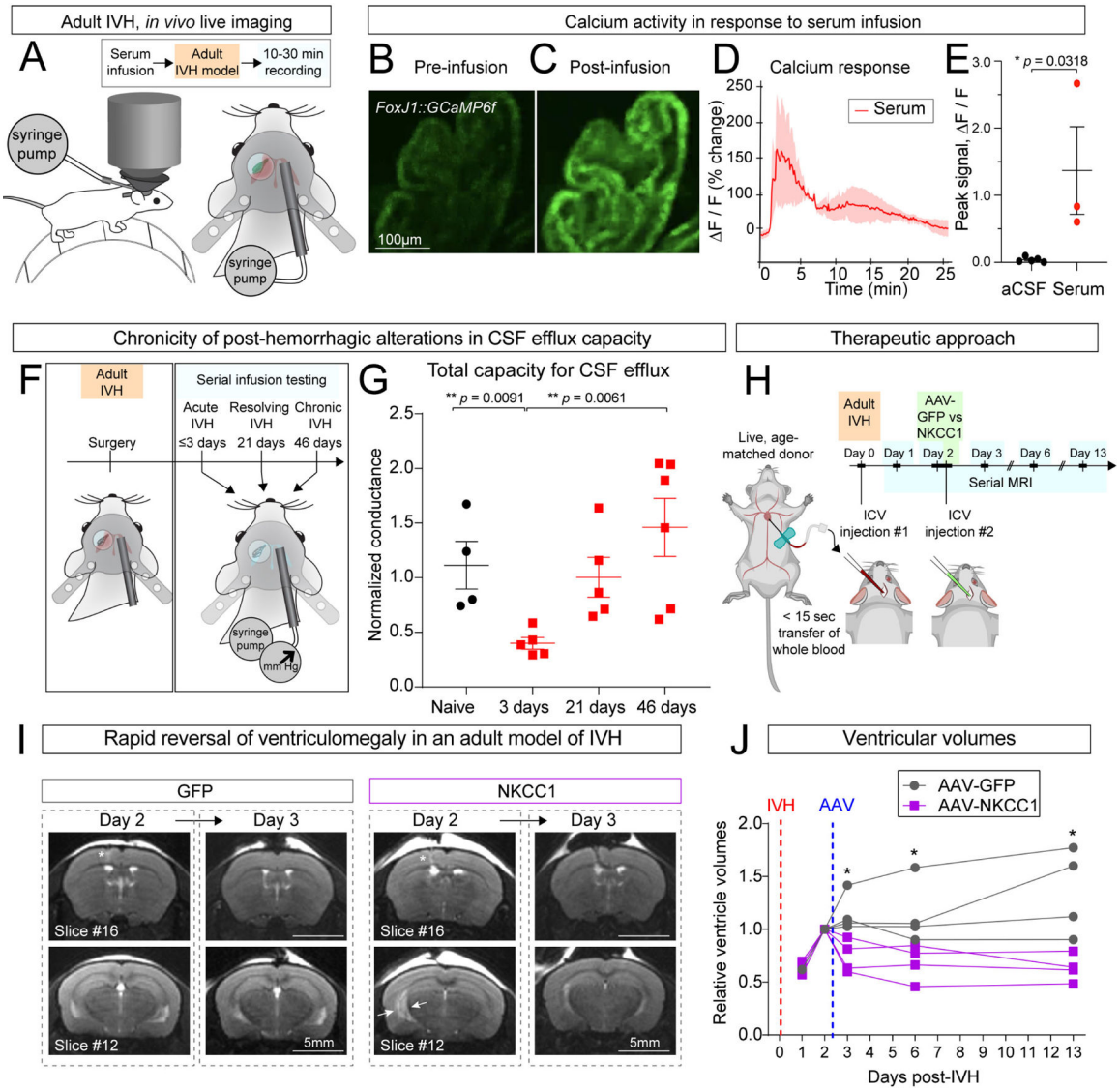

Figure 5. Adult mouse model of PHH mirrors key aspects of pediatric PHH and responds to ChP-NKCC1 therapy.

(**A**) Schematic depicting devices and surgical implantation for *in vivo* ChP live-imaging with two-photon microscopy. (**B-C**) Calcium responses to serum in ChP epithelial cells (*FoxJ1-Cre::GCaMP6f* mice) *in vivo*. Scale bar = 100 μm. (**D-E**) Representative fluorescence intensity trace with serum infusion and quantification of peak intensity. aCSF N = 4, serum N = 3. * $p = 0.0318$. Welch's two-tailed unpaired t-test. Data presented as mean ± SD. (**F**) Schematic depicting adult IVH serial infusion test post-IVH. (**G**) Adult CSF clearance capacity post-IVH measured by infusion test. Naïve: N = 3, 3 days: N = 5, 21 days: N = 5, 46 days: N = 6. ** $p = 0.0091$, ** $p = 0.0061$. Welch's two-tailed unpaired t-test. Data presented as mean ± SD. (**H**) Schematic depicting the therapeutic approach in adult PHH model and the time-course of serial MRI. (**I**) Representative T2-MRI images showing rapid reversal of ventriculomegaly in adult PHH model by ChP-NKCC1 overexpression. AAV-GFP was used as control. Scale = 5 mm. (**J**) Relative ventricular volume in adult PHH

mice with AAV-NKCC1 treatment or control. For each mouse, the ventricular volumes on different days were normalized to the value of Day 2 post-IVH, immediately prior to AAV transduction. N = 4, * $p < 0.05$ (Day 3: $p = 0.0138$; Day 6: $p = 0.0386$; Day 13: $p = 0.0152$). Data analyzed by multiple t-test and corrected for multiple comparisons using Holm-Sidak method. Each data point represents one mouse.

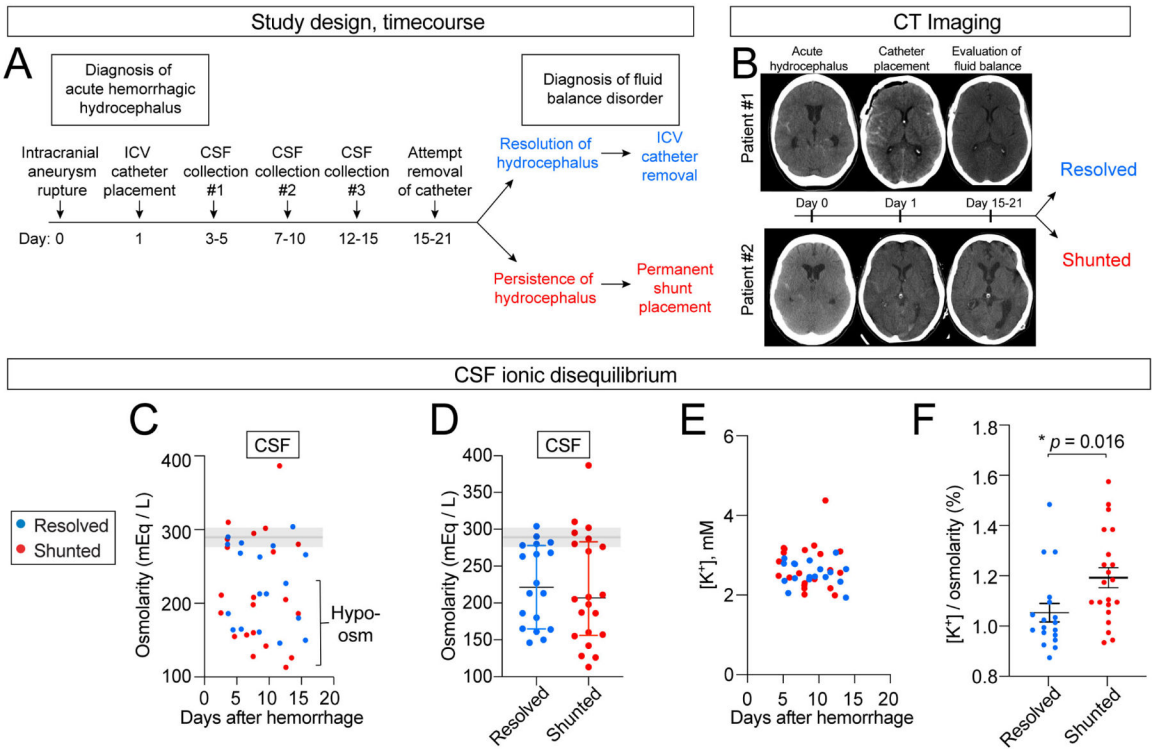

Figure 6. Adult human CSF shows positive correlation between post-SAH / IVH ionic disturbance and shunted outcome.

(**A**) Study design. (**B**) Representative CT images from patients with resolved (#1) vs. shunted (#2) hydrocephalus. (**C-D**) CSF osmolarity decreased in some CSF samples regardless of disease course. Shaded area shows 95% normal values.[74] Blue: resolved, N = 18 (7 patients, 2–3 timepoints per patients). Red: shunted, N = 21 (8 patients, 2–3 timepoints per patient). (**E-F**) Absolute CSF [K^+] was not altered but relative CSF [K^+] to total osmolarity was higher in individuals requiring permanent shunting vs. individuals who recovered and had initial ventricular catheter removed. Blue: resolved, N = 18 (7 patients, 2–3 timepoints per patients). Red: shunted, N = 21 (8 patients, 2–3 timepoints per patient). * $p = 0.016$. Welch's two-tailed unpaired t-test. All data presented as mean ± SD. Each data point represents one CSF sample collected from one patient at a single timepoint.

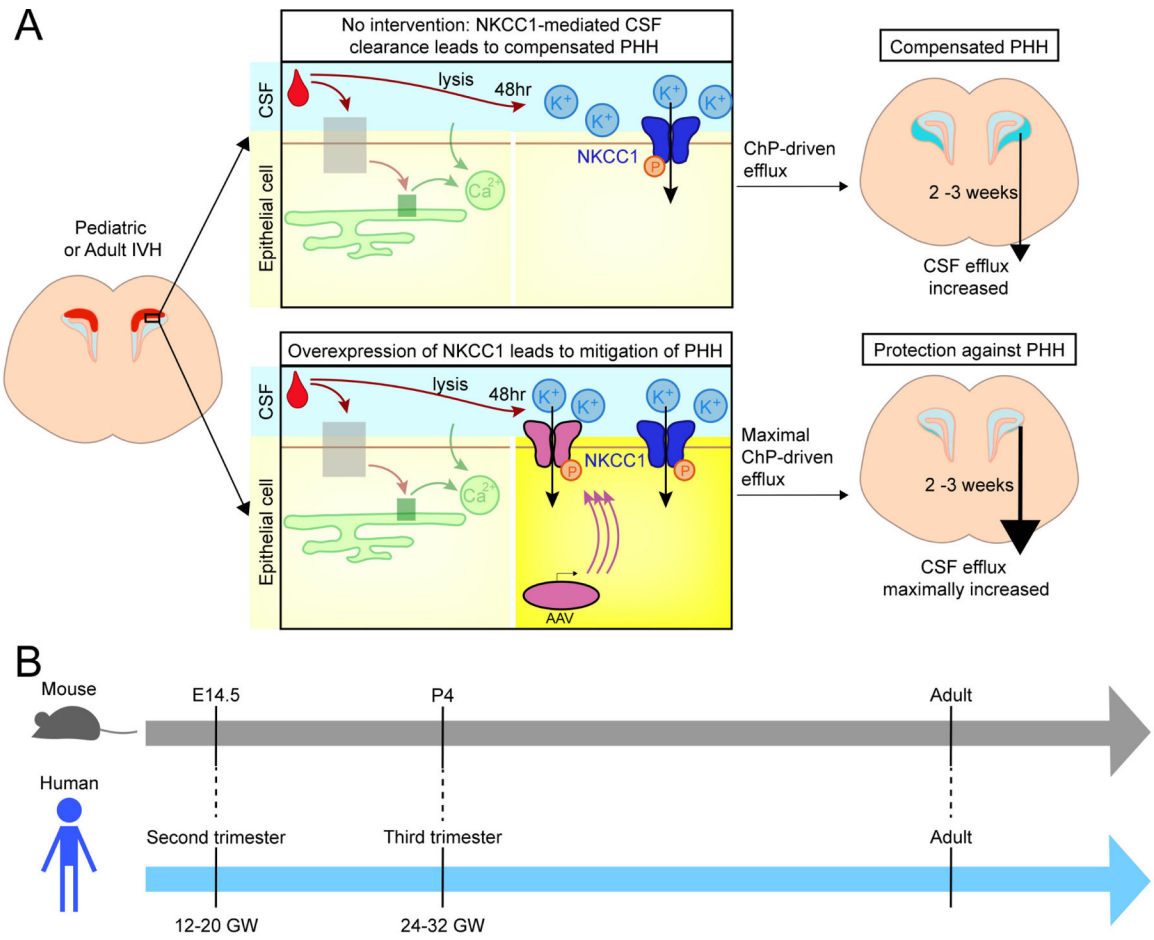

Figure 7. ChP compensatory actions in PHH.

(**A**) Two scenarios of ChP activities following IVH. *Upper panels*: The ChP responds to blood with acute calcium activation. After 48 hrs, CSF-[K^+] increases. With elevated CSF-[K^+], NKCC1 activation leads to net flux of ions and osmotically obliged water movement from CSF into ChP, resulting in compensated PHH characterized by mild ventriculomegaly and enhanced CSF clearance capacity. *Lower panels:* AAV-mediated overexpression of NKCC1 enhances the total amount of Na^+-K^+−$2Cl^-$ cotransport, preventing ventriculomegaly. (**B**) Mouse and human developmental timelines[35].

KEY RESOURCES TABLE

REAGENT or RESOURCE	SOURCE	IDENTIFIER
Antibodies		
Rabbit anti-NKCC1	Abcam	ab59791; RRID: AB_944433
Rabbit anti-pNKCC1	EMD Millipore	ABS1004; RRID: N/A
Rabbit anti-GAPDH	Sigma	G9545; RRID: AB_796208
Mouse anti-HA	Abcam	ab130275; RRID: AB_11156884
Rat anti-HA	Roche	11867423001; RRID: AB_390918
Rabbit anti-FLAG	Abcam	ab1162; RRID: AB_298215
Rabbit anti-Iba1	WAKO	019-19741; RRID: AB_839504
Rat anti-CD68	Abcam	ab53444; RRID: AB_869007
Bacterial and Virus Strains		
AAV2/5-NKCC1	Modified from Somasekharan et al.[54]	Addgene plasmid #49077
AAV2/5-NKCC1-NT51	Modified from Somasekharan et al.[54]	Addgene plasmid #49061
AAV2/5-GFP	Boston Children's Hospital viral core, IDDRC	N/A
Biological Samples		
Human CSF	Massachusetts General Hospital	N/A
Chemicals, Peptides, and Recombinant Proteins		
Paraformaldehyde	Sigma	P6148
EGTA	Sigma	E3889
BAPTA-AM	Tocris	2787
2-APB	Tocris	1224
LiCl	Sigma	203637
Clarity™ Western ECL Substrate	BioRad	170-5060
Critical Commercial Assays		
Deposited Data		
Blood proteomics	ProteomeXchange Consortium via the PRIDE partner repository	PXD039738
Experimental models: Cell lines		
Experimental Models: Organisms/Strains		
CD-1 IGS Mouse (referred to as CD-1)	Charles River Laboratories	Strain code: 022
FoxJ1-CRE	Zhang et al.[76]	N/A
Ai95D(RCL-GCaMP6f)-D	Jackson Laboratory	028865; RRID:IMSR_JAX:028865
Oligonucleotides		

REAGENT or RESOURCE	SOURCE	IDENTIFIER
Recombinant DNA		
Software and Algorithms		
Prism	GraphPad	v7
FIJI/ImageJ	Schindelin et al.[84]	http://imagej.net/Fiji;https://imagej.nih.gov
ZEN Black/Blue	Zeiss	N/A
AMIDE	https://amide.sourceforge.net/	N/A
MatLab	Mathworks	R2019b
Other		